Timelapse photogrammetry reveals hydrological controls of finescale HighArctic glacier surface roughness evolution

Irvine-Fynn, Tristram D.L.; Holt, Tom O.; James, Timothy D.; Smith, Mark W.; Rutter, Nick; Porter, Philip R.; Hodson, Andrew J.

Published in:
Earth Surface Processes and Landforms

DOI:
10.1002/esp.5339
10.1002/esp.5339

Publication date:
2022

Citation for published version (APA):
Irvine-Fynn, T. D. L., Holt, T. O., James, T. D., Smith, M. W., Rutter, N., Porter, P. R., & Hodson, A. J. (2022). Timelapse photogrammetry reveals hydrological controls of finescale HighArctic glacier surface roughness evolution. *Earth Surface Processes and Landforms*, *47*(6), 1635-1652. https://doi.org/10.1002/esp.5339, https://doi.org/10.1002/esp.5339

Received: 31 July 2021 | Revised: 24 December 2021 | Accepted: 30 December 2021

DOI: 10.1002/esp.5339

RESEARCH ARTICLE

ESPL WILEY

Time-lapse photogrammetry reveals hydrological controls of fine-scale High-Arctic glacier surface roughness evolution

Tristram D. L. Irvine-Fynn[1] | Tom O. Holt[1] | Timothy D. James[2] | Mark W. Smith[3] | Nick Rutter[4] | Philip R. Porter[5] | Andrew J. Hodson[6,7]

[1]Department of Geography and Earth Sciences, Aberystwyth University, Aberystwyth, UK

[2]Department of Geography and Planning, Queen's University, Kingston, Ontario, Canada

[3]School of Geography, University of Leeds, Leeds, UK

[4]Department of Geography and Environmental Sciences, Northumbria University, Newcastle, UK

[5]School of Life and Medical Sciences, University of Hertfordshire, Hatfield, UK

[6]Department of Arctic Geology, University Centre in Svalbard (UNIS), Longyearbyen, Norway

[7]Department of Environmental Sciences, Western Norway University of Applied Sciences, Sogndal, Norway

Correspondence
Tristram Irvine-Fynn, Department of Geography and Earth Sciences, Aberystwyth University, Aberystwyth, SY23 3DB, UK.
Email: tdi@aber.ac.uk

Funding information
Royal Geographical Society; University Centre in Svalbard (UNIS); Climate Change Consortium of Wales, Grant/Award Number: C3W; Leverhulme Trust, Grant/Award Number: RF-2018-584/4

Abstract

In a warming Arctic, as glacier snowlines rise, short- to medium-term increases in seasonal bare-ice extent are forecast for the next few decades. These changes will enhance the importance of turbulent energy fluxes for surface ablation and glacier mass balance. Turbulent energy exchanges at the ice surface are conditioned by its topography, or roughness, which has been hypothesized to be controlled by supraglacial hydrology at the glacier scale. However, current understanding of the dynamics in surface topography, and the role of drainage development, remains incomplete, particularly for the transition between seasonal snow cover and well-developed, weathered bare-ice. Using time-lapse photogrammetry, we report a daily timeseries of fine (millimetre)-scale supraglacial topography at a 2 m^2 plot on the Lower Foxfonna glacier, Svalbard, over two 9-day periods in 2011. We show traditional kernel-based morphometric descriptions of roughness were ineffective in describing temporal change, but indicated fine-scale albedo feedbacks at depths of ~60 mm contributed to conditioning surface topography. We found profile-based and two-dimensional estimates of roughness revealed temporal change, and the aerodynamic roughness parameter, z_0, showed a 22–32% decrease from ~1 mm following the exposure of bare-ice, and a subsequent 72–77% increase. Using geostatistical techniques, we identified 'hole effect' properties in the surface elevation semivariograms, and demonstrated that hydrological drivers control the plot-scale topography: degradation of superimposed ice reduces roughness while the inception of braided rills initiates a subsequent development and amplification of topography. Our study presents an analytical framework for future studies that interrogate the coupling between ice surface roughness and hydro-meteorological variables and seek to improve parameterizations of topographically evolving bare-ice areas.

KEYWORDS
glacier surface, hydrology, photogrammetry, roughness, semivariance

1 | INTRODUCTION

Across the Arctic region, glacier equilibrium lines are rising (Curley et al., 2021; Noël et al., 2019, 2020; Ryan et al., 2019). Consequently, over the coming few decades, the spatial extent of bare-ice during the ablation season is expected to increase as the glaciers thin and recede (Huss & Hock, 2015). The rate of melting in these bare-ice areas is controlled by the radiative and turbulent energy fluxes, which are regulated, respectively, by the ice surface's albedo and topography (Hock, 2005). In many continental glacierized locations radiative fluxes dominate the surface energy balance (~77%); however, in climate regimes where cloud cover is commonplace, the turbulent fluxes become more substantial contributors, accounting for up to 80% of the energy available for ablation (Willis et al., 2002). Phases of

elevated turbulent energy fluxes are commonly associated with synoptic 'melt events', which are often coupled with rainfall, or occur during the ablation-to-accumulation season transition period (e.g., Doyle et al., 2015; Fausto et al., 2016; Giesen et al., 2014; Gillett & Cullen, 2011; Hay & Fitzharris, 1988). With observations and forecasts of amplified warming in the Arctic (e.g., Overland et al., 2019), increasing synoptic rainfall events (Bintanja, 2018; Bintanja et al., 2020), and an underestimation of cloud feedbacks (e.g., Middlemas et al., 2020), future projections of the region's glacier mass balance demand improved spatial and temporal parameterizations of ice topography and turbulent energy fluxes.

Melting glacier bare-ice surface topography is complex and dynamic. This variability, at the local scale, is driven by spatially differing ablation caused by crystal anisotropy (e.g., Greuell & de Wildt, 1999); emergent ice structures (e.g., Hambrey & Lawson, 2000; Hudleston, 2015; Jennings & Hambrey, 2021); non-stationary impurities (including dust and cryoconite: e.g., Gribbon, 1979; Bøggild et al., 2010; Irvine-Fynn et al., 2011; Nield et al., 2013; Takeuchi et al., 2018); and incipient surface hydrology and 'micro-channels' (Bash & Moorman, 2020; Mantelli et al., 2015; Rippin et al., 2015). However, synoptic influences further complicate the evolution of topography: for example, surface morphology can be reduced or eliminated during periods of enhanced turbulent energy fluxes and/or rainfall-driven conductive and latent heat exchanges (Liu et al., 2020; Müller & Keeler, 1969; Takeuchi et al., 2018). Such close coupling between dynamic glacier surface characteristics and hydrometeorology offers an explanation for the contrasting reports of spatial and temporal trends in topographic variability, with examples of systematic evolution (e.g., Guo et al., 2011; Herzfeld et al., 2003; Liu et al., 2020; Smeets & van den Broeke, 2008) countered by descriptions of incoherent change (e.g., Brock et al., 2006; Guo et al., 2018). Reconciling these contrary perspectives, Smith et al. (2020) suggested that, at the deci- to deca-metre patch- or plot-scales, the temporal change in bare-ice surface topography is unordered, yet is organized and predictable at larger (glacier) scales, primarily owing to the progressive evolution of the supraglacial hydrological system.

Surface topography is commonly described by its texture or roughness and, of the many representations or metrics (Smith, 2014), the aerodynamic roughness length (z_0) is commonly used to estimate the turbulent energy flux in numerical models of glacier ice melt (Hock, 2005). Defined as the boundary layer height above the glacier surface at which wind velocity reduces to zero, z_0 typically lies at the millimetre-scale over ablating bare-ice, but can vary over several orders of magnitude (Brock et al., 2006, and references cited therein). Because turbulent energy fluxes are proportional to the square of the natural logarithm of z_0, an increase in z_0 from 2.2 to 5.5 mm can increase turbulent energy available for ice melt by 20% (Brock et al., 2006). Yet, despite the recent increase in studies reporting bare-ice z_0 (e.g., Brock et al., 2006; Chambers et al., 2020, 2021; Fitzpatrick et al., 2019; Guo et al., 2011; Guo et al., 2018; Irvine-Fynn et al., 2014b; Rees & Arnold, 2006; Smeets et al., 1999; Smeets & van den Broeke, 2008; Smith et al., 2016), the understanding of how glacier surface topography and z_0 varies over space and time, at a range of scales, remains incomplete (e.g., Liu et al., 2020; Smith et al., 2020). This is particularly the case for the trajectory of bare-ice as it transitions from superimposed ice with discrete residual snow patches to a mature surface topography defined by hydrology.

The relative paucity of quantifications of heterogenous, emergent glacier bare-ice surface roughness presents a persistent research challenge. Fitzpatrick et al. (2019) concluded that topographic representations at ~1 m horizontal resolution are required to define bare-ice roughness features, z_0, and, by inference, surface processes. Such a fine-scale lies below the resolution of many satellite-retrieved products used to monitor or represent glacier surface characteristics (Chambers et al., 2021). Consequently, many numerical melt models use either time-constant values based on published estimates or tune the z_0 roughness value to fit observed ablation or runoff observations (e.g., Arnold et al., 2006; Fausto et al., 2016; Giesen et al., 2014; Østby et al., 2017). These simplifications fail to reproduce the turbulent energy fluxes in a realistic manner (Hock, 2005), and prompt the continued desire for refinement of current parameterizations of z_0 in glacier and ice sheet surface energy balance models (e.g., van den Broeke et al., 2017).

The spatial and temporal roughness patterns at metre to submetre scales can be informative not only for z_0 but of dynamical processes, interactions, and feedbacks at the surface (Herzfeld et al., 2000). However, these insightful length-scales correspond to those of supraglacial rill and stream widths and their spacing, cryoconite holes, foliation and other ice structure, and, importantly, to the scale-dependency of ice surface roughness between length-scales of 0.1 to ~2 m (Rees & Arnold, 2006). Nonetheless, roughness variability at finer scales is essential to inform the response of, and uncertainties in data retrieved from assorted satellite platforms (Fitzpatrick et al., 2019; Rees & Arnold, 2006; van Tiggelen et al., 2021). Yet, despite such critical questions, assessments of bare-ice topographic dynamics, and their drivers, at high resolution remain lacking.

The capability of time-lapse imaging and modern photogrammetric methods to reveal fine-scale ice surface topographic change is evident in recent glaciological investigations (e.g., Bash et al., 2018; Bash & Moorman, 2020; Rippin et al., 2015; Ryan et al., 2015; Rossini et al., 2018), and exemplified by retrievals of fine-scale bare-ice topography (e.g., Irvine-Fynn et al., 2014b; Liu et al., 2020; Smith et al., 2016; Smith et al., 2020). However, there remain relatively few studies that identify or verify processes defining surface roughness and seek to improve the parameterization of z_0. Here, we contribute to this research gap by presenting a novel, low-cost framework involving time-lapse photogrammetry to interrogate a fine-scale surface microtopography time-series, and explore the role of hydrology in conditioning glacier surface roughness at a High-Arctic site over two 9-day periods in 2011.

2 | FIELD SITE AND METHODS

Svalbard harbours ~5% of Earth's glacier ice volume outside Greenland or Antarctica (Martín-Español et al., 2015), and is getting warmer and wetter (Hanssen-Bauer et al., 2019), with rising seasonal snowlines and increased bare glacier ice extents during summer months (Noël et al., 2020). In this climate-sensitive, glacierized locality, at Foxfonna (78.1°N, 16.2°E) we generated fine (millimetre)-scale surface elevation models for a bare-ice plot to explore the temporal dynamism of roughness, which defines the turbulent energy exchanges at the glacier surface and holds relevance for summer mass balance across the changing Arctic region.

2.1 | Foxfonna

Foxfonna is a small, high-elevation ice cap complex, which extends over < 10 km^2 to ~820 m above sea level (a.s.l.), with two principal outlet glaciers discharging ice to lower elevations: the increasingly disconnected Rieperbreen to the west, and Lower Foxfonna to the north (Christiansen et al., 2005; Rutter et al., 2011). Lower Foxfonna is assumed to be cold-based, despite ice thicknesses of up to 125 m (Christiansen et al., 2005; Liestøl, 1974), with surface elevations ranging from ~380 to 700 m a.s.l. where the glacier is fed by an icefall descending from the ice cap (Figure 1a). The Lower Foxfonna glacier flows northwest towards a large boulder moraine ridge, bifurcating into two narrow tongues that extend to the north and northwest, respectively.

During the melt season in 2011, we instrumented the larger, ~1.3 km^2 north-western portion of the glacier and monitored a 9 m^2 surface observation plot with a time lapse camera array. The summer melt season at the site is characterized by persistent positive air temperatures typically lasting for ~60 days, from mid-June to mid-August (Rutter et al., 2011). However, as is typical in western Svalbard, cloud cover occurs for at least 55% of the summer season, and snowfall is not uncommon (Hanssen-Bauer et al., 1990). In 2011, residual seasonal snow remained across much of the Lower Foxfonna glacier surface until mid-July, with the subsequent decay of slush over 3 days exposing superimposed ice and glacier ice over the lower elevations from around 21 July (day of year [DOY] 202).

2.2 | Hydrometeorological data collection

Local meteorology for the study site was recorded at an automatic weather station (AWS) installed at 601 m a.s.l. on Lower Foxfonna. The Campbell Scientific AWS recorded incident radiation (SW_{in}: ±10%); the 2 m air temperature (T_a: ±0.35°C); wind speed (±0.3 m s^{-1}) that was assumed to be dominantly katabatic and down-glacier; relative humidity (±6%); and the distance-to-ice-surface (±0.4%) using a 22° field-of-view ultrasonic depth sounder. All meteorological data were logged as hourly averages of 1 min measurement sampling, and distance-to-ice was recorded discretely each hour as the mean of 10 pulses. All sensors were maintained at heights of between 1.5 and 2.5 m above the ice surface. To eliminate noise in the ultrasonic sensor record, a simple 6-h running mean was used to smooth the ice ablation data, following application of the manufacturer's temperature correction factor. Precipitation (with an accuracy of ±8%) was acquired at 12-h intervals from ~18 km northwest of Foxfonna at Svalbard Lufthaven (available at www.eklima.no).

From the AWS data, we estimated the energy balance at our observation plot following Brock and Arnold's (2000) point-based approach adjusted for high latitudes (see Irvine-Fynn et al., 2014a). Briefly, the model estimates net short- and long-wave radiation, sensible heat, and latent heat fluxes at a point at hourly time-steps using inputs of observed irradiance, air temperature, windspeed and derived saturated vapour pressure. Additional geometric data (e.g., latitude, elevation, slope, and aspect), elevation difference between point of interest and the location of the input meteorological records, and ice albedo and aerodynamic roughness can be prescribed. Subsurface heat conduction is excluded from the model. Incident radiation and wind speed at the AWS were assumed to be representative for our observation plot, particularly as terrain shadowing is not explicitly accounted for, while saturation vapour pressure was assumed to hold an empirical relationship with relative humidity and air temperature (Irvine-Fynn et al., 2014a). To describe the air temperature at the plot elevation of ~492 m a.s.l., we employed three Gemini TinyTag air temperature loggers in aspirated housings (precision: ±0.4°C) over the lower part of the glacier (see Figure 1a). From DOY 200 to DOY 240, hourly T_a and the three TinyTag records were highly correlated ($0.844 < r < 0.961$; $P < 0.05$), and revealed a mean linear lapse rate of −0.011°C m^{-1} at the hourly time-step between 454 and 601 m a.s.l.

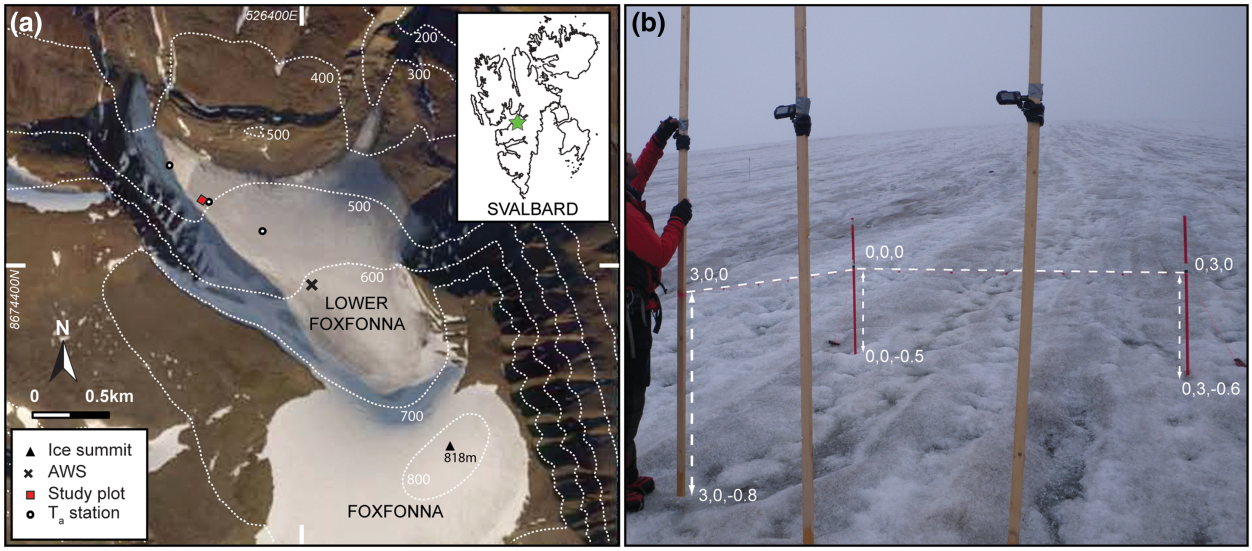

FIGURE 1 (a) Map detailing Lower Foxfonna's setting and topography, and the locations of the 9 m^2 observation plot with a time lapse camera array, the automatic weather station (AWS), and the TinyTag air temperature stations during 2011. The background orthophoto from 2006 was made available by Store Norske Spitsbergen Kulkompani AS. Foxfonna's location in central west Svalbard is shown in the inset. (b) Image of the observation plot, looking up-glacier, illustrating the convergent camera set-up and reference markers with approximate scales and distances shown for the arbitrary coordinate system employed (photograph credit: Arwyn Edwards) [Color figure can be viewed at wileyonlinelibrary.com]

Air temperature at the observation plot was estimated from T_a using a time-varied, linear lapse rate derived for each hour.

Advancing the energy balance model to incorporate time-evolving surface properties, we incorporated our photogrammetric data to describe the albedo (α) and aerodynamic roughness (z_0) at the observation plot (see Section 2.4). Lastly, while anticipated to be small, we estimated the additional melt generated by precipitation at the plot using the regional 17.5% per 100 m lapse rate (van Pelt et al., 2016). We assumed that over the 12-h measurement intervals, precipitation fell at (i) a steady rate, and (ii) the corresponding positive mean 2 m air temperature at the observation plot; we discounted precipitation during periods where air temperatures were ≤ 0°C (see Hock, 2005).

2.3 | Digital image acquisition and photogrammetric processing

At the subjectively typical mid-glacier plot site, we targeted the transitional time-period that follows the demise of seasonal snow-cover, as residual snow and superimposed ice degrades, and bare glacier ice is exposed and subject to increased melt. We advanced the image acquisition methods described by Irvine-Fynn et al. (2014b) to record the evolving ice surface topography. Specifically, three 14 Mpix Pentax Optio WG-1 cameras in time-lapse mode were installed to provide red-green-blue (RGB) stereo images of the observation plot, with redundancy (Figure 1b). The Optio cameras capture 4288 × 3216 pixel JPEG images with a bit depth of 24, using a CCD sensor (6.2 mm × 4.6 mm) with a focal length range of 28 to 140 mm and maximum aperture of F3.5–5.5. The cameras were mounted on wooden poles ~0.95 m apart, drilled into the ice to depth of ~1.5 m, and oriented up-glacier with convergent optical axes ~45° from nadir to minimize camera calibration errors (Wackrow & Chandler, 2008). Images were captured automatically every hour over a 4-week period from 27 July to 22 August (DOYs 208–234), using auto-focus mode with an auto-digital ISO 80-400 setting, amplified sharpness, and no flash.

An important requirement of photogrammetry is the placement of ground control points (GCPs) within the overlapping camera field of view. The GCPs account for any movement in the cameras as well as tying the resulting digital surface models (DSMs) to a defined coordinate system. As there was no stable surface on which to install GCPs, an arbitrary coordinate system was defined using a taut level string initially affixed ~0.5 m above the ice surface between the northern-most camera pole and two plastic poles drilled into the ice at 3 m spacing and surrounding the observation plot. Markers were placed every 0.5 m along the string and used as control points (Figure 1b). This rudimentary approach provided a simple way to tie our surface models to an arbitrary coordinate system; however, any movement of the poles over time would cause deviations in the GCP positions that would translate into absolute positional errors in the derived DSMs. While we mitigated these errors by monitoring and re-surveying the GCP positions regularly (every 2 to 3 days), their influence on our results was expected to be minimal since our analysis focused only on relative changes in surface relief. Moreover, any GCP drift caused by ice ablation would be gradual over time and thus errors between sequential models would be small even if the GCP movement was significant over time. Finally, while placement of all GCPs on the same plane is not ideal, robust camera calibration and tightly constraining the models to the encompassing GCP network helped to maximize the relative quality of neighbouring DSMs in the time series, though this is more important for change detection analysis than for comparisons of surface roughness. We anticipated and found that these surface changes and the relief were large compared to any resulting relative error in the DSMs (see later).

Ice ablation during the observation period necessitated adjustment of the time lapse camera array on 1 August and 13 August (DOYs 213 and 225): these major amendments in GCP geometry were recorded manually with an estimated uncertainty of 5 mm and 2°. Owing to a combination of misty conditions or snow and camera lens icing that reduced visibility in the images, and camera tilt that became problematic for adequately resolving the GCPs, imagery between 5 August and 12 August (DOYs 217 and 224) was discarded from the analyses. Following initial photogrammetric checks, optimal lighting conditions for derivation of DSMs and orthomosaics were found to be at 18:00 local time, and so one DSM was generated per day at this time.

Camera calibration and photogrammetric processing to produce the DSMs from the time-lapse imagery were undertaken in Topcon's ImageMaster Pro. For further details on oblique photogrammetric processing, see Wolf and Dewitt (2000). Without independent means of measuring the ice surface topography or GCP geometry, it was not possible to fully quantify error in the DSMs. However, the block (or bundle) adjustment results provide an indication of the photogrammetric fit to the final rasterized solution. Here, mean horizontal DSM fit was estimated to be ~2 mm with resolution along the optical axis of 2 mm. Vertical precision was lower, and also included the millimetre-scale catenary error associated with the control point set-up (Irvine-Fynn et al., 2014b). Nonetheless, with the source image resolution, we estimated that a conservative, vertical sub-centimetre uncertainty remained (see Irvine-Fynn et al., 2014b; Smith & Vericat, 2015), which lay below the anticipated daily ablation (Rutter et al., 2011). The DSMs were resampled to a 5 mm horizontal resolution across the observation plot.

2.4 | Derivation of glacier surface metrics

To describe the changing morphology of a 1.5 m × 1.5 m (2.25 m^2) common area across the 17 rasterized DSMs that were generated for the observation plot, using a kernel equivalent to 5 × 5 pixels (0.025 m resolution or 1×10^{-4} m^2) we extracted three roughness metrics, averaged across the plot: the relative position of topography (Jenness, 2006), standard deviation of elevations (Ascione et al., 2008), and Riley's terrain ruggedness index which describes the elevation difference between adjacent DSM cells (Riley et al., 1999).

For comparison, we then extracted elevation data profiles from the common area, oriented cross- and down-glacier at 5 mm intervals. Each individual profile was linearly detrended, and the following standard soil science roughness metrics were calculated, then averaged for the plot (after Irvine-Fynn et al., 2014b): the standard error of elevation or effective roughness height (the random roughness: Allmaras et al., 1966); the absolute sum of slopes (Currence & Lovely, 1970); and a microrelief index that is based on the maximum angle from the horizontal between measured elevation points (Romkens & Wang, 1986). In glaciology, the bulk aerodynamic approach that uses

topographic profiles and Lettau's (1969) physical approximation (see Brock et al., 2006; Munro, 1989) is a commonplace and satisfactory method (Chambers et al., 2020) to estimate z_0. Therefore, we derived roughness lengths (z_{0M}) from the detrended cross- and down-glacier profiles. Negligible difference in the magnitude and patterns retrieved for each of the topographic metrics was found following a reduction of the data sampling resolution to 10 mm, corresponding to the finest resolution required for adequate representation of roughness (Rees & Arnold, 2006).

Removal of larger-scale trends (e.g., overarching plot slope) is crucial for more robust evaluations of surface roughness (James et al., 2007). Therefore, to further our analyses, we used a two-dimensional linear detrend to remove overarching surface slope signatures for each DSM. From each of these detrended DSMs, we calculated the bearing area curve, which is the cumulative distribution function of the detrended elevations, and derived a *z*-score histogram. Lastly, following the two-dimensional method detailed in Smith et al. (2016), we determined two cross-glacier and two down-glacier estimates for each DSM, which accounts for upwind frontal area to calculate an alternative aerodynamic roughness length estimate (z_{0S}). Assuming z_{0S} to be a more robust measure of the bulk aerodynamic roughness compared to z_{0M} (see Smith et al., 2016), we then used these mean cross- and down-glacier metrics for each DSM to derive a surface anisotropy index (Ω: after Smith et al. [2006]).

To examine the frequency and orientation of any glacier surface roughness signals in the detrended DSMs, we applied long-standing spectral and geostatistical approaches (e.g., Herzfeld et al., 2000; Mulla, 1988; Rees & Arnold, 2006). Initially, we employed a two-dimensional fast Fourier-transform to retrieve a frequency domain depiction of the amplitude of topographic variations in cross- and down-glacier directions (e.g., Perron et al., 2008; Spagnolo et al., 2017); the detrended DSM data were used without further adjustment or filtering. Subsequently, we computed the overall spatial autocorrelation (or omnidirectional semivariograms) from detrended elevation values extracted from 2000 randomly located points distributed across each of the detrended DSMs. For comparison, each of the semivariograms were normalized to the associated detrended elevation variance. The analysis was restricted to a maximum lag distance of ~0.75 m, as defined by the plot scale. Guided by the results of the Fourier-transform (see Section 3.2), to explore directional contrast in spatial autocorrelation, we recalculated directional semivariograms for each of the DSMs using the two, perpendicular directions of cross- and down-glacier, with a 30° tolerance.

To enhance the energy balance modelling at the observation plot using a temporally varying albedo, we determined the apparent cryoconite area with ImageJ software (Schneider et al., 2012), using pixel thresholding of the blue band of the daily orthophotographs (see Irvine-Fynn et al., 2011). The apparent cryoconite area was converted to an albedo proxy following the relationship reported by Irvine-Fynn et al. (2011) for Longyearbreen, a similarly north-facing glacier proximate to Foxfonna; cubic interpolation of these discrete, daily time-points provided an hourly estimate of surface albedo at intervals, and the observed mean of 0.62 was used for the periods before and after the time-lapse imaging. With knowledge that katabatic winds are dominant over Lower Foxfonna (unpublished data), we prescribed a time-varied aerodynamic roughness length in the model using the mean plot-scale cross-glacier profile (z_{0M}) at 18:00 each day, estimating z_0 at hourly time-steps over the observation period with a cubic interpolation. For the time-periods before and after the imaging periods, z_0 was fixed as the mean DSM-derived cross-glacier z_{0M}. We note that our time-varying estimates of albedo and roughness are not fully validated, and so while representing 'best estimates' they introduce some uncertainty in the melt model outputs.

3 | RESULTS

3.1 | Lower Foxfonna's hydrometeorology

Figure 2(a–e) summarizes the summertime meteorological conditions on Lower Foxfonna in 2011. Over the imaging period, T_a remained low with a mean of 3.4°C, and 52% of the days being classed as cloudy with maximum daily SW_{in} < 400 Wm^{-2}. Ice ablation at the AWS typically reached 27 mm d^{-1} (0.025 m w.e. d^{-1}). The observation period was characterized by two phases separated by a precipitation event (DOYs 223–224): the first phase becoming increasingly overcast over time, with declining air temperature, low wind speed, and high humidity (DOYs 208–222); the second, with rising irradiance and air temperature, elevated winds, and comparatively lower humidity (DOYs 225–234). These two contrasting phases also broadly coincided with the two sets of reconstructed DSMs derived from the plot, hereafter referred to as observation subperiods (OSP) 1 and 2 (Figure 2g). Both imaging periods began with discrete patches of residual snow on the glacier surface that took approximately 48 h to clear and expose bare-ice.

The numerically simulated melt over 12-h periods, corresponding to the precipitation record interval, was highly correlated to observed ablation ($r = 0.97$). Advected energy from rainfall was negligible, accounting for less than 0.1 mm w.e. d^{-1}, owing to low air temperature and temporally averaged precipitation intensity. OSP1 was characterized by proportionally high radiative fluxes (Figure 2f), with only minor contributions from turbulent energy, because although air temperatures were relatively high ($T_a \approx 5$°C), wind speeds remained low (typically < 2 m s^{-1}). In the latter stages of OSP1, melt rates declined from DOYs 214–216 as both incident radiation and air temperature declined. In contrast, OSP2 began with 3 days of net energy loss by the glacier (i.e., no melt), and the following 5 days (DOYs 228–232) exhibited more balanced contributions to ablation from radiative and turbulent energy fluxes, with elevated air temperature (T_a < 5°C) and wind speed (~2.5 m s^{-1}), which subsequently declined.

3.2 | Fine-scale surface topography and roughness

Our photogrammetric approach yielded 17 fine-scale DSMs and orthomosaics describing the ice surface at the observation plot (Figure 3a). Throughout the DSM time-series, the ice surface topography changed (Figure 3b–d). The seventeen 5 mm horizontal resolution DSMs revealed the plot was typically characterized by a mean relief of 0.26 m, with a standard deviation of 0.055 m. Daily differencing of the DSMs over the common area showed a maximum elevation change of −0.115 m d^{-1}; however, recognizing the spatial uncertainties within the DSMs, using a 5 × 5 pixel kernel, the mean relief

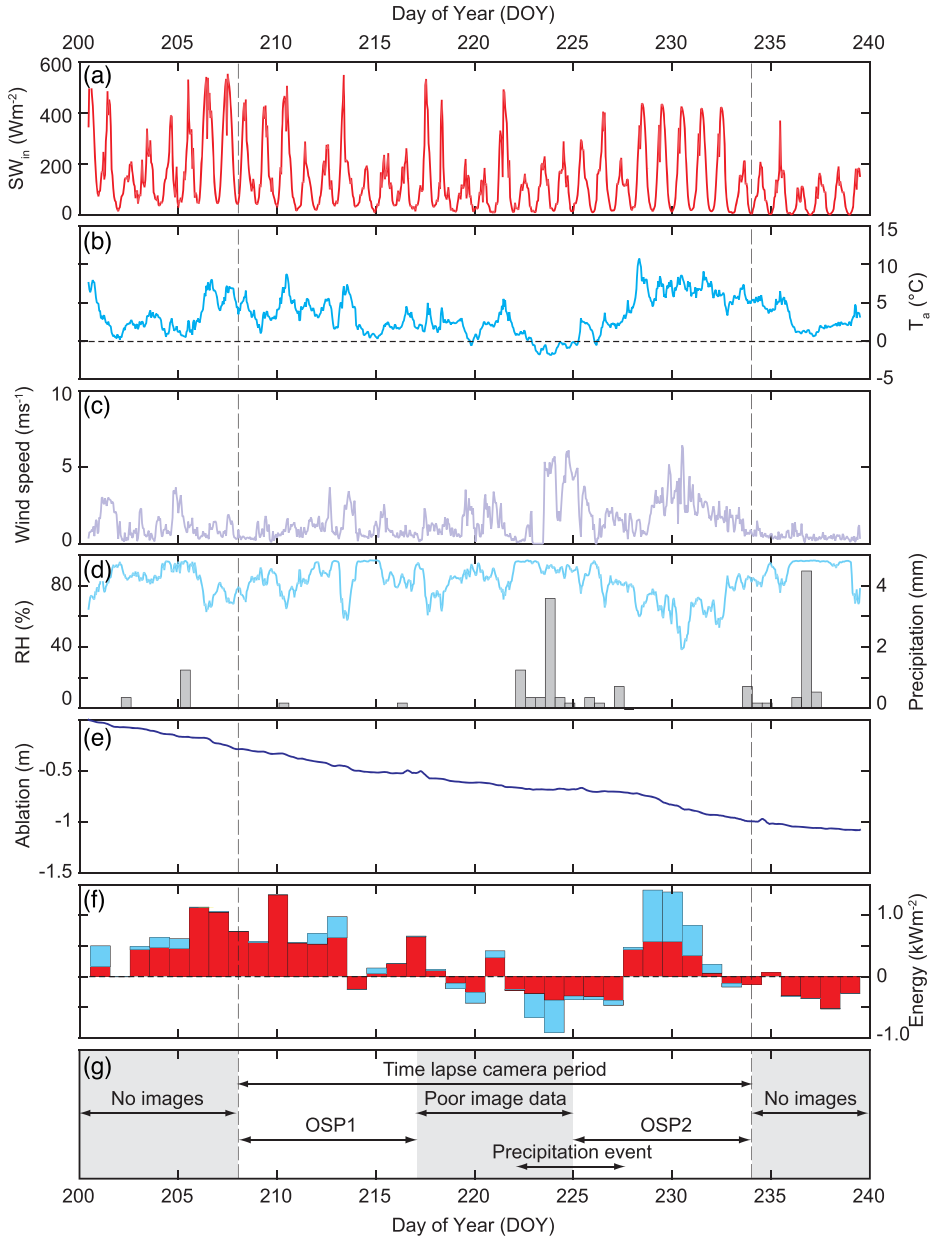

FIGURE 2 Time-series of hydrometeorological conditions at the observation plot on lower Foxfonna, illustrating: (a) incident radiation, SW_{in}; (b) air temperature at 2 m, T_a; (c) wind speed; (d) relative humidity (RH) and precipitation (grey bars); (e) cumulative ice ablation; (f) modelled surface energy balance, with bars indicating total daily energy receipt separated into radiative (red) and turbulent (blue) fluxes, with negative values indicative of periods exhibiting energy lost from the glacier to the atmosphere; and (g) schematic chart of image data acquisition, the two OSPs and notable meteorological phases [Color figure can be viewed at wileyonlinelibrary.com]

decreased to 0.24 (± 0.055) m with a maximum ablation of 0.092 m w.e. d^{-1}. Across the common area over the observation period, the DSMs revealed a mean ablation of 0.028 m w.e. d^{-1} (Figure 4a,b), which equalled that reported at the weather station (Section 3.1; Figure 2e).

The mean DSM pixel scale slope varied over a 5.5° range throughout the OSPs, but the mean aspect and the traditional kernel-based morphological metrics remained constant over time (Figure 4c–f). Owing to its dependence on kernel-scale slope, Riley's topographic ruggedness index showed subtle variation centred at ~0.23 m (Figure 4g). As source images were not colour-calibrated and the camera automatically adjusted the F-stop, ISO and exposure time, the temporal pattern in the RGB brightness was challenging to interpret (Figure 4i); however, the blue-band brightness, as an albedo proxy (see Irvine-Fynn et al., 2011), suggested a declining surface reflectance during OSP1, and subsequently a subtle increase during OSP2 (Figure 4h). For the individual DSMs, correlations between kernel-based surface descriptors and the associated melt rate were generally weak ($|r| < 0.1$) but highly varied, with both positive and negative spatial correlations ($-1 < r < 0.98$) depending on the day of observation, and with no identifiable difference between OSP1 and OSP2 (Figure 5). Elevation change at the kernel-scale, between sequential DSMs, was not consistently correlated to any ice surface descriptor for the first DSM of each pair (Figure 5).

The variability in surface topography and roughness (Figures 3 and 4) over the OSPs was better evidenced by the profile-based metrics, with directional difference evident between the cross- and down-glacier directions (Figure 6a–e). The cross-glacier random roughness and microrelief indices were 17% to 88% greater than their counterparts oriented down-glacier; for z_{0M} this directional contrast was greater at 38% to 180%. These relative directional disparities were most pronounced during OSP2 (from DOY 229). A similar contrast was seen in z_{0S}, with down-glacier values being 17% to 30% greater than the cross-glacier direction. With the exception of the sum of slopes, temporal decline characterized the cross-glacier profile-based roughness metrics over the OSP1, which then increased during OSP2. The ΣS metric lacked clear, systematic variations over time which suggested that the surface texture remained broadly

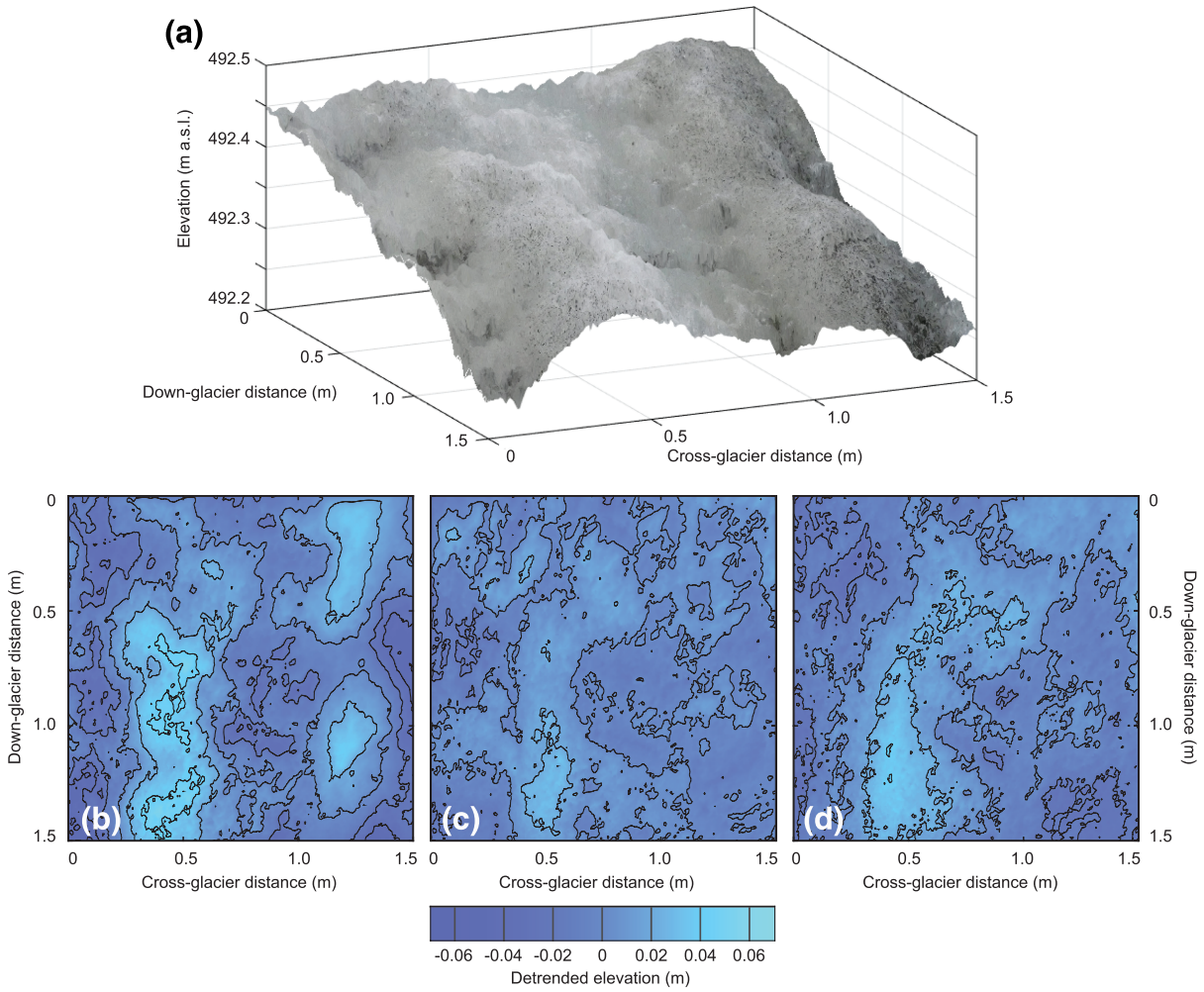

FIGURE 3 (a) Example three-dimensional visualization of the 2.25 m^2 common area at the observation plot for DOY 213 retrieved following our photogrammetric workflow; the 5 mm resolution DSM, with vertical exaggeration, is overlain by the coincident 2 mm orthomosaic and highlights fine-scale morphology and the presence of impurities across the plot. Shaded contour plots for the two-dimensionally detrended DSMs retrieved for (b) DOY 213, (c) DOY 225, and (d) DOY 233 illustrating the evolving topography of the bare-ice surface. Note the reduction in plot's topography between 1.0 and 1.5 m in the cross-glacier direction [Color figure can be viewed at wileyonlinelibrary.com]

similar throughout the OSPs. The detrended DSMs revealed the observation plot surface was weakly anisotropic, with cross-glacier roughness z_{0S} consistently greater than equivalent down-glacier values ($-0.13 < \Omega < -0.07$). A seasonal trend in Ω with a significant increase over time ($r^2 = 0.79$; $P < 0.01$; $n = 17$) showed the surface became progressively more isotropic (Figure 6f).

Examining the time-series of roughness metrics (Figures 4 and 6), cross-glacier profile-based metrics were all positively correlated: Spearman's $\rho > 0.77$, $P < 0.01$. Of the kernel-based metrics, only the Riley's ruggedness index showed strong, positive association with the profile-based cross-glacier roughness metrics ($0.74 < \rho < 0.84$; $P < 0.01$). Speculating that glacier roughness increases under radiative-driven melt, and decreases under turbulent fluxes (Müller & Keeler, 1969), from the melt model output we derived these two cumulative energy fluxes for 24-h intervals preceding each DSM, and the associated turbulent: radiative energy flux ratio. Table 1 illustrates how the profile-derived random roughness, microrelief index and z_{0M}, and the z_{0S} metrics were all significantly correlated to both the daily cumulative radiative energy ($0.50 < \rho < 0.66$; $P < 0.05$), and the blue-band brightness ($0.60 < \rho < 0.93$; $P < 0.02$). However, only the kernel-based relative position of topography metric showed significant association with cumulative turbulent energy and the turbulent: radiative energy ratio ($\rho > 0.7$; $P < 0.01$).

Once bare-ice was exposed in OSP1, z_{0M} decreased over time ($r^2 = 0.87$; $P < 0.01$), but this was coincident with a decline in the radiative energy over the same timescale ($r^2 = 0.44$; $P < 0.05$). Conversely, over OSP2, z_{0M} increased ($r^2 = 0.77$; $P < 0.01$) but concurrent increases in daily radiative or turbulent fluxes were insignificant ($r^2 < 0.08$; $P > 0.2$). The temporal trends in z_{0S} were similarly significant in both OSPs. During OSP1, the difference between cross- and down-glacier z_{0M} decreased by 0.05 mm d^{-1} indicative of a smoothing of the ice surface; for z_{0S}, this decline was 0.025 mm d^{-1}. In comparison, during OSP2 the directional difference rose by only 0.03 mm d^{-1} for z_{0S} and 0.01 mm d^{-1} for z_{0M}.

The bearing area curves (Figure 7a) showed a broad similarity in form, typically with the lower 50% of the detrended elevation range occupying only between 19% and 47% of the total area, with exception to the two outermost curves (DOYs 225 and 228). The slightly positive elevation skew revealed by the bearing area curves was clear in the corresponding *z*-score histograms (Figure 7b): a *z*-test confirmed that all the detrended DSMs statistically followed a normal distribution ($|z| < 1.15 \times 10^{-11}$; $P < 0.01$) although there is a higher

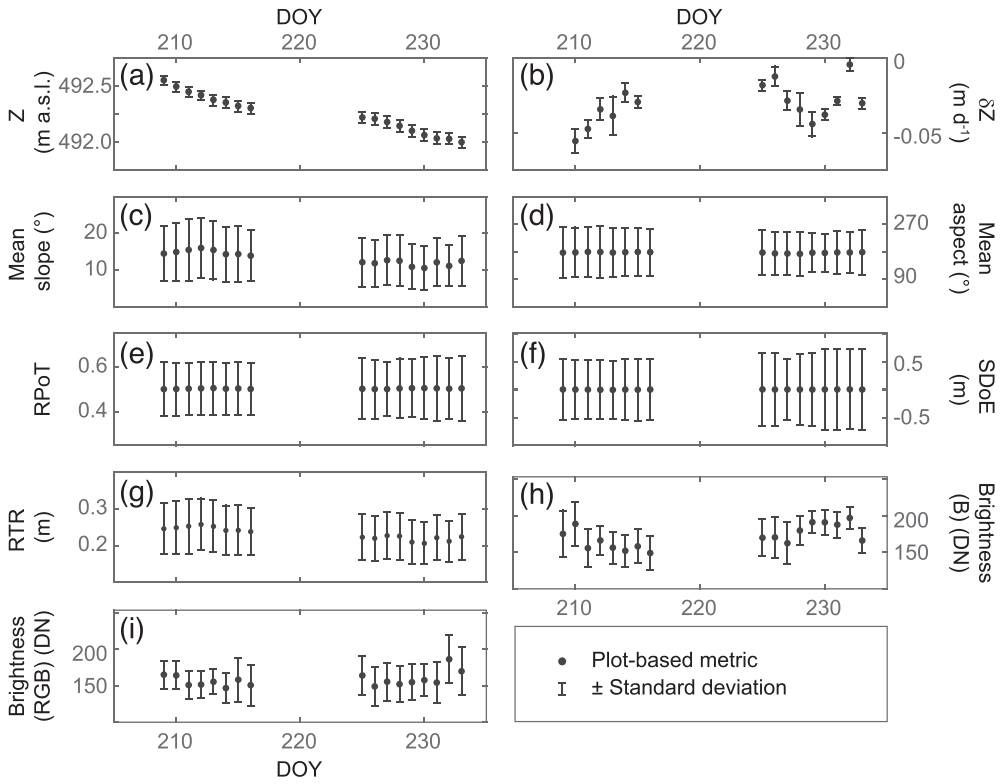

FIGURE 4 Kernel-based elevation, roughness and brightness metrics across the observation plot's common area, and their variation over time during OSP1 and OSP2. (a) Surface elevation based on GCPs for OSP1 and OSP2, noting the elevation data is not continuous between the OSPs; (b) ice surface elevation change for the preceding 24-h period; (c) mean surface slope over the observation plot; (d) mean surface aspect; (e) position of topographic roughness, RPoT; (f) standard deviation of elevation, SDoE; (g) Riley's topographic ruggedness index, RTR; (h) blue-band othomosaic brightness reported as a digital number (DN); and (i) RGB orthomosaic brightness (DN). Error bars are given as ± 1 × standard deviation

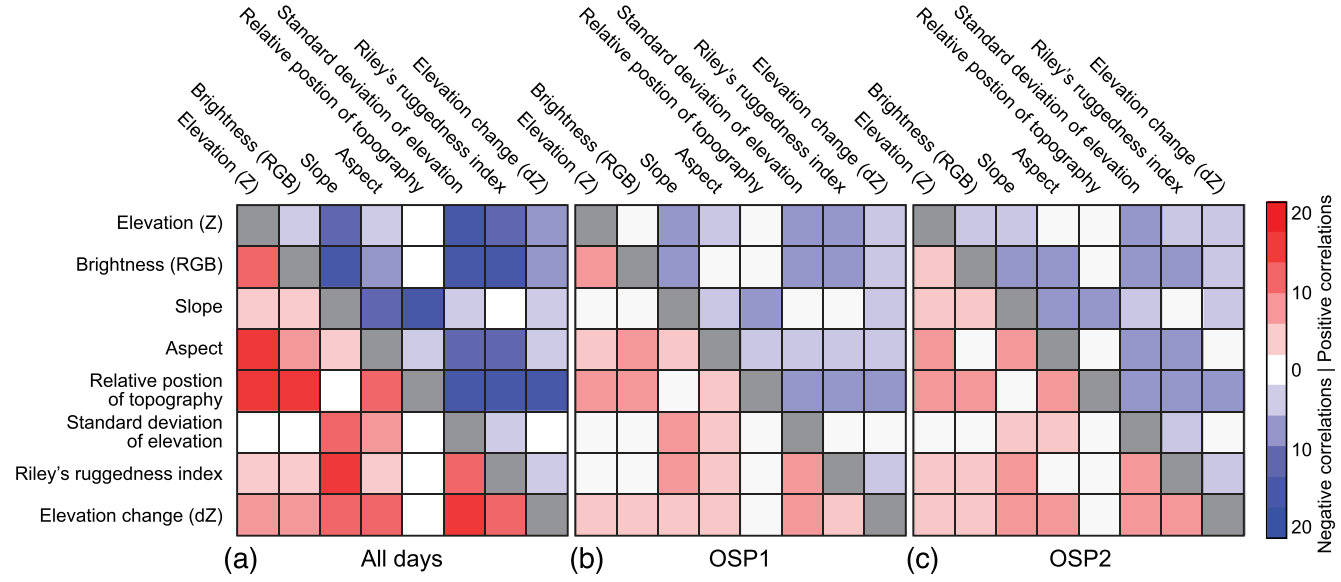

FIGURE 5 Illustration of the number of positive and negative correlations between all of the kernel-based DSM surface metrics and surface change (dZ) for (a) the observation period, (b) OSP1 and (C) OSP2 [Color figure can be viewed at wileyonlinelibrary.com]

probability that a point in the detrended DSM surface lies between 0 and +1 standard deviation of the detrended elevation range, equivalent to approximately 0 to 16 mm above the generalized mean surface plain. There was some variability seen in the *z*-score plot suggestive of topographic variability at intermediate depths (0.8 to 32 mm) below the generalized surface plane.

The two-dimensional Fourier-transform consistently showed highest power in the centre of the Fourier domain (Figure 8a–c), corresponding to low frequency signals and gradual changes in the glacier surface topography. Critically, the orientation of any dominant periodicity in the topography would produce perpendicular lines in the Fourier power plots. The absence of any oblique patterns in the Fourier power surfaces (Figure 8), suggested topographic periodicity in the detrended DSMs was oriented in the plot's cross- and down-glacier directions. The relative power of these two perpendicular signals was diminished for DOYs 225 and 233 (Figure 8b,c), indicative of a reduced topographic variability during OSP2.

With regard to spatial autocorrelation in surface topography, the omnidirectional semivariograms, derived from the detrended DSMs, showed a contrast between OSP1 and OSP2 (Figure 9a,b). During OSP1, the semivariograms showed similar form, with a lag distance of

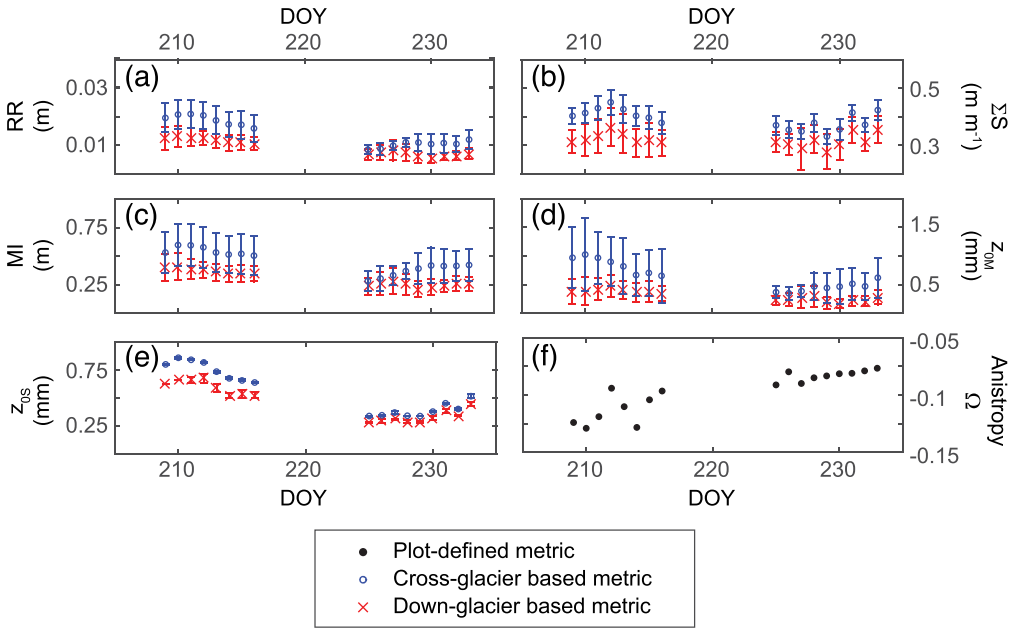

FIGURE 6 Profile-derived and two-dimensional roughness metrics, and their variation over time. (a) Random roughness, RR; (b) absolute sum of slopes, Σ*S*; (c) microrelief index, MI; (d) profile-based bulk aerodynamic roughness estimate, z_{0M}; (e) two-dimensional aerodynamic roughness estimate, z_{0S}; and (f) anisotropic index, Ω, derived from cross- and down-glacier z_{0S}. Error bars are given as ± 1 × standard deviation [Color figure can be viewed at wileyonlinelibrary.com]

TABLE 1 Correlation matrix for daily energy flux proxies and mean observation plot roughness measures. Correlations are reported with the Spearman's ρ-value, and those which are significant at the 95% confidence level are italicized and shaded. Cumulative incident radiation and turbulent energy, and the turbulent-to-radiative energy flux ratio for the 24-h periods between each digital surface model (DSM) are denoted ΣRad_{24}, $\Sigma Turb_{24}$ and $[T:R]_{24}$, respectively. Brightness was extracted from both the red-green-blue (RGB) and blue-band orthomosaics of the observation plot

Variable	ΣRad_{24}	$\Sigma Turb_{24}$	$[T:R]_{24}$	Brightness (RGB)	Brightness (blue)
$\Sigma Turb_{24}$	0.19				
$[T:R]_{24}$	*0.60*	*0.59*			
Brightness (RGB)	0.09	−0.04	0.06		
Brightness (blue)	*0.65*	0.01	0.17	0.03	
Relative position of topography	0.42	*0.72*	*0.71*	0.02	0.05
Standard deviation of elevation	−0.31	−0.06	−0.10	0.45	*−0.49*
Riley's topographic ruggedness	0.31	−0.36	−0.26	−0.17	*0.70*
Random roughness	*0.61*	−0.17	0.08	−0.11	*0.85*
Sum of slopes	0.38	0.00	−0.02	−0.07	*0.60*
Microrelief index	*0.66*	−0.07	0.10	0.02	*0.92*
z_{0M}	*0.60*	−0.18	0.07	0.08	*0.90*
z_{0S}	*0.50*	−0.17	−0.11	−0.01	*0.88*
Anisotropy, Ω	−0.39	0.44	0.19	0.18	*−0.72*

0.43 and 0.49 m to the peak semivariance of 0.00045 (±0.0001) m^2. For OSP2, the peak semivariance was reduced, at 0.00015 ($\pm 5.5 \times 10^{-5}$) m^2, and the associated lag distance varied from 0.37 to < 0.73 m. However, none of the individual semivariograms could be modelled using monotonically-increasing spherical, exponential or Gaussian model functions (e.g., Rees & Arnold, 2006; Ryan et al., 2017b).

With roughness metrics (Figure 6) and the two-dimensional Fourier power spectrum (Figure 8) confirming the topographic signals aligned with the cross- and down-glacier geometry, the directional semivariograms cross- and down-plot revealed a 'hole effect' semivariogram model (Journel & Huijbregts, 1978; Pyrcz & Deutsch, 2003). During OSP1, the cross-glacier empirical semivariograms peaked at a lag distance of ~0.4 m, falling thereafter with the suggestion of a cyclical form at lag distances < 0.7 m (Figure 9c); the down-glacier semivariance, in contrast, tended to approach a sill at a lag distance of ~0.5 m (Figure 9e). During OSP2, the shape of the semivariograms was less coherent, with cross-glacier semivariograms continuing to increase or showing indications of some variability at lag distances > 0.4 m (Figure 9d); in the down-glacier direction, some days exhibited monotonic increase towards the overall plot semivariance at ranges > 0.6 m, while others (snow-affected DOYs 225–227) displayed semivariance peaks at lag distances of ~0.4 m (Figure 9f).

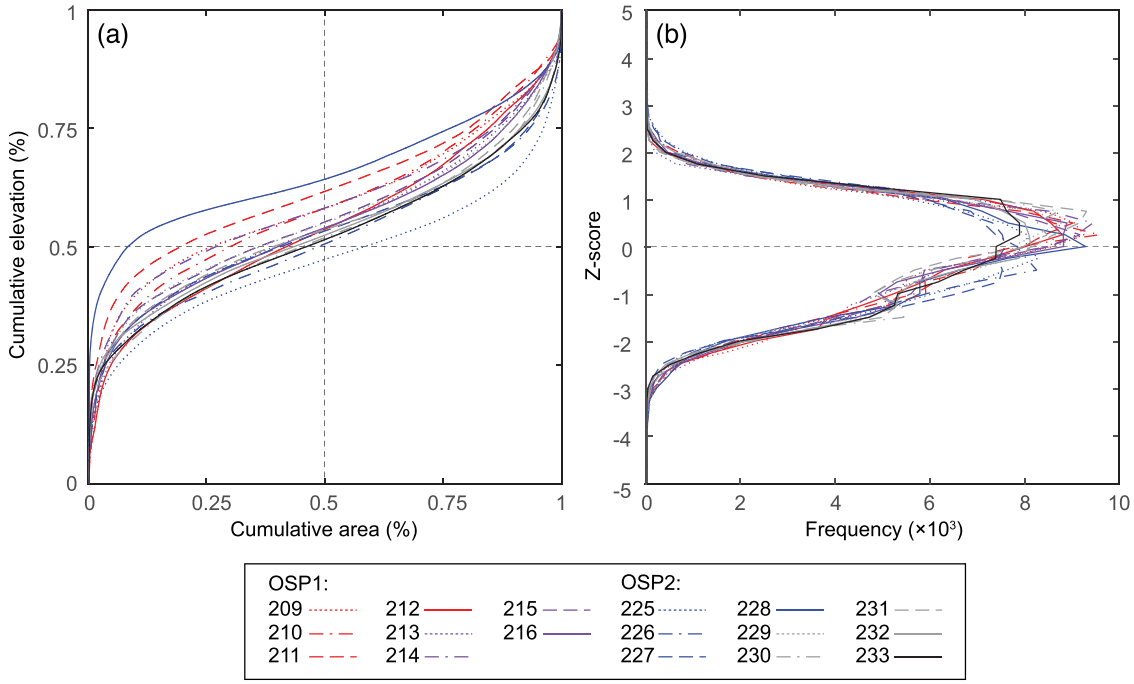

FIGURE 7 (a) Bearing area curves for each detrended DSM and (b) detrended DSM z-score histograms, showing an absence of any systematic change over time. Curves are plotted for each of the 17 detrended DSMs, indicated for each DOY [Color figure can be viewed at wileyonlinelibrary.com]

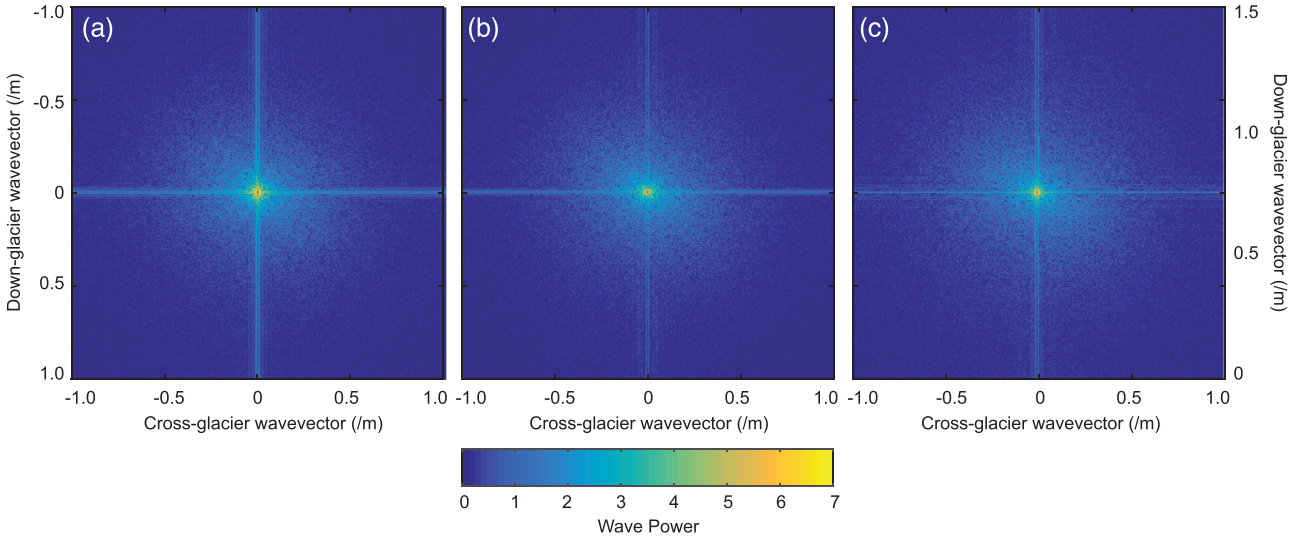

FIGURE 8 Plots of the two-dimensional Fourier-transform of the detrended DSMs retrieved on (a) DOY 213, (b) DOY 225, and (c) DOY 233, highlighting the absence of any topographic signal oblique to the cross- and down-glacier directions [Color figure can be viewed at wileyonlinelibrary.com]

4 | DISCUSSION

Conventional understanding of bare-ice topographic development suggests that roughness increases over the melt season following the elimination of seasonal snow as the ice surface degrades and supra-glacial channels and hummocks are established (Smith et al., 2020). We, therefore, examine our microtopographic data from Lower Foxfonna for the two, contrasting time-periods, OSP1 and OSP2, within this context.

4.1 | Hydrometeorology, ablation and roughness

We observed daily bare-ice microtopography over 2 week-long periods: OSP1 was dominated by radiative energy fluxes, while OSP2 exhibited a higher proportion of turbulent energy fluxes, compared to OSP1. Over the full observation period, the AWS recorded ice ablation rates of 25 mm w.e. d^{-1}. These rates were reproduced by the differencing of the time-series of photogrammetrically-derived DSMs (28 mm w.e. d^{-1}), and demonstrated the robustness of the

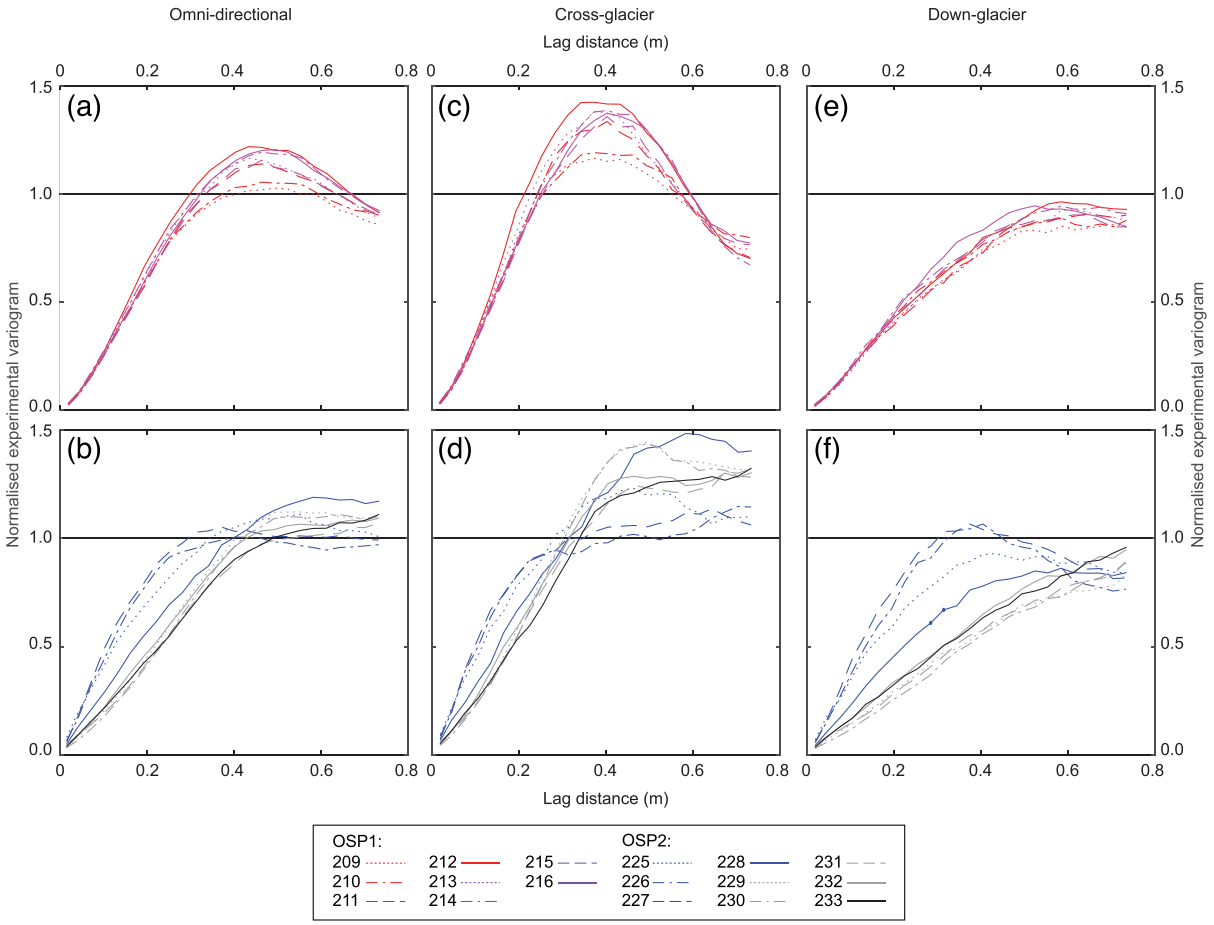

FIGURE 9 Variance-normalized empirical semivariograms derived for the detrended DSMs generated for OSP1 and OSP2: omnidirectional semivariograms for OPS1 (a) and OSP2 (b); cross-glacier semivariograms for OSP1 (c) and OSP2 (d); and down-glacier semivariograms for OSP1 (e) and OSP2 (f). Semivariograms are reported for each DOY within the OSPs. Note: DOYs 209, 210, 225–227 were affected by declining patches of residual snow over the observation plot [Color figure can be viewed at wileyonlinelibrary.com]

methodological approach, acknowledging the associated uncertainties. The ablation forecast over the same time by the point-based energy balance, despite being highly correlated to observed surface lowering, over-predicted the observed melt by ~30%. This discrepancy is explained by the cold thermal regime that Foxfonna exhibits: energy is lost to subsurface conduction (e.g., Arnold et al., 2006; Østby et al., 2017). Such losses are not accounted for in the melt model employed to estimate radiative and turbulent energy contributions, and so are not examined further here.

Our analytical approach demonstrated that traditional kernel-based measures, which classed the bare-ice surface as smooth or flat, offer limited insight into spatial and temporal topographic variability that the profile-based or two-dimensional assessments reveal. Examination of metrics derived from 1×1 to 9×9 pixel kernels emphasized that increased kernel size reduced the range and variability reported by each metric: a scale-dependent behaviour well known in geomorphology (e.g., Brasington et al., 2012). Previous work has employed an adapted standard deviation of elevation over large kernels to report glacier surface roughness (e.g., Rippin et al., 2015; Rossini et al., 2018). However, the potential for such measures to reveal morphological change over time is unclear. Here, particularly for bare-ice surface areas, we suggest that more thorough scaling analyses of surface roughness are needed (e.g., Chambers et al., 2021; Fitzpatrick et al., 2019; Smith et al., 2020). Owing to the scale-dependence of both ice roughness itself (Rees & Arnold, 2006) and traditionally employed roughness metrics, multi-scale approaches should be explored (e.g., Lindsay et al., 2015, 2019), specifically to discern and describe temporal change, or relate ground validation to coarser resolution satellite data retrievals.

The nature of the variability of the surface topography was not readily explained by the geometries and metrics describing the DSMs or the orthomosaics, highlighting the complexity of the evolution of bare-ice topography and contrasts in the meteorology during the two OSPs. Processes such as the lateral advection and redistribution of meltwater (Bash & Moorman, 2020; Mantelli et al., 2015) or impurities (Chandler et al., 2015; Irvine-Fynn et al., 2011; Takeuchi et al., 2018) occur at length-scales greater than the 25 mm kernel and over time-scales below our daily observation period. However, there were indications of the apparent influence of discrete impurities on surface roughness. The blue-band brightness typically offers strong discrimination between impurities and ice (see Irvine-Fynn et al., 2010). Across the plot, the profile-based roughness metrics, and daily radiative energy receipt and blue-band brightness changed concurrently: such an association can be explained by the melting in or emergence of impurities (Bøggild et al., 2010; Gribbon, 1979; Takeuchi et al., 2018) and their visibility from the oblique imaging geometry,

and the presence of meltwater. This process is supported by the variability in the elevation distributions with the changes at depths of up to 60 mm from the ice surface. Such depths accord with those of small cryoconite holes and supraglacial rills observed elsewhere in Svalbard (e.g., Rippin et al., 2015; Telling et al., 2012). Because brightness was not normalized across the orthomosaic time-series, nor corrected for local shadowing (e.g., Leidman et al., 2021), a more robust image calibration (e.g., Ryan et al., 2017a, 2017b; Tedstone et al., 2020) approach would be required to strengthen these tentative spatio-temporal albedo and roughness associations.

4.2 | Aerodynamic roughness length evolution

Our data revealed mean estimates of z_0 < 1.5 mm, with anisotropy evident in dissimilar down- and cross-glacier evaluations, as previously reported for glacier ice (e.g., Brock et al., 2006; Fitzpatrick et al., 2019; Guo et al., 2011; Irvine-Fynn et al., 2014b; Liu et al., 2020; Smith et al., 2016). The profile-derived and two-dimensional roughness metrics demonstrated evolution during both OSPs, with rates of change in z_0 that compare well to those reported by Smith et al. (2020), and our data demonstrate the trajectory of roughness as the glacier surface transitions from residual snow and superimposed ice to bare-ice. To explain the decline then subsequent rise in surface roughness on Lower Foxfonna, we employ a five-stage conceptual model of the development of surface features (after Guo et al., 2011; Smith et al., 2020): residual, melting snow roughness increases (stage 1), then, here, following the exposure of bare-ice on DOY 209, z_0 initially declines (stage 2), subsequently beginning to increase as the melt season continues and bare-ice degrades (stage 3), and then progressively develops a more hummocky form (stages 4). It remains unclear if our observations reveal the bare-ice's seasonal 'peak roughness' (stage 5: Smith et al., 2020).

On glaciers across Svalbard, superimposed ice commonly forms early in the melt season, and is subsequently exposed and degraded as ablation progresses (Wadham & Nuttall, 2002). On Lower Foxfonna, in 2011, immediately prior to the demise of the snowpack in late July (DOY 202: see Section 2.1) superimposed ice had formed and been preserved with a thickness of ~0.2 m (Koziol et al., 2019). This friable superimposed ice layer comprised ice lenses and cryoconite distributed below ~55% of its depth. During OSP1 (stage 2), through a combination of refreezing within the degrading superimposed ice layer and the subsequent progressive exposure of the underlying glacier ice, the topography appeared to smoothen. This (stage 2) trajectory was also promoted by the simultaneous decrease in radiative energy flux, which would reduce the likelihood of differential ablation arising from impurity or ice-structural albedo-feedbacks. The elevated estimated plot albedo (~0.62: see Section 2.4) when compared to more typical values of ~0.4 for glacier ice (Cuffey & Paterson, 2010), offered further evidence of a superimposed ice dominated stage.

The timing of the precipitation event, which included snowfall at the time-lapse camera array site, and the resulting data quality issues prevented us from describing the topographic changes as superimposed ice was eliminated (stage 3). However, at the start of OSP2, residual snow cover affected the topography of the plot, most clearly evident in the bearing area curve. As OSP2 progressed (stage 4), increasing roughness was driven by the sustained energy fluxes and, with turbulent fluxes dominant, spatially varied ablation arose from the surface feedbacks associated with rill development and the progressive roughening of the ice surface.

The importance of the observed changes in z_0 were best illustrated with subsequent melt model runs, that compared the dynamic albedo and z_{0M} roughness parameterization to scenarios with z_0 set as a constant: using the minimum recorded cross-glacier z_{0M} and z_{0S}, throughout the observation period, melt due to turbulent energy at an hourly timescale was underestimated on average by approximately 7%, while for the equivalent maximum values this was a 10–15% overestimate. These disparities in turbulent energy fluxes translated to a typical mean uncertainty in predicted hourly ablation of up to 10%.

4.3 | Hydrological drivers of ice surface roughness

Identification of the hole effect in the semivariograms derived from the detrended DSMs implies that there is an underlying form of cyclicity or structure in the topography at the plot-scale (Pyrcz & Deutsch, 2003). Here, the interpretation of the cyclical signature in the cross-glacier semivariogram, and supressed down-glacier semivariogram, is that throughout OSP1, the glacier surface was characterized by down-glacier oriented ridges, spaced at ~0.8 m intervals. The period was defined by a low turbulent-to-radiative energy ratio, and the location exhibits ice structure parallel to the surface slope, with foliation and/or antecedent topography at the observation plot broadly oriented down-glacier (Figure 10a). The orientation of apparent ridges aligned with the surface slope and structure may also control (i) the distribution of impurities, and (ii) the local thickness of superimposed ice, its internal drainage and meltwater refreezing. Such controlling factors maintain a down-glacier oriented topography throughout OSP1, whilst accommodating the declining roughness and anisotropy.

In contrast, OSP2 showed a differing semivariogram form, with a dampened or absent cyclicity in the cross-glacier direction and, in the down-glacier direction, either an apparent sill at lag distances > 0.8 m or tentative suggestions of cyclicity on the residual snow affected days. These semivariogram forms are suggestive of regular or irregular lenses or 'islands' on the surface (Pyrcz & Deutsch, 2003). Here, the semivariograms were interpreted to indicate the surface topography evolved from structurally-controlled ridges in OSP1 to upstanding islands 0.4 m to 0.8 m long in the down-glacier direction and 0.5 m in the cross-glacier direction in OSP2 (Figure 10b). However, these islands appeared to be quasi-transient, decaying as residual snow melted and OSP2 progressed further. While turbulent energy comprised a higher proportion of the total melt energy during this phase, ablation was less governed by albedo and likely more spatially uniform, but with melt rates remaining low, the ablating glacier ice likely experienced development of distributed rills and micro-channels, which progressively migrated over the surface (Bash & Moorman, 2020; Mantelli et al., 2015; Rippin et al., 2015). Such rills would be conducive to the formation of the transient ice islands; as ablation continues, these rills are subject to increasing meltwater fluxes, and (re-)establish a slope- or structure-defined drainage network thereby increasing surface roughness.

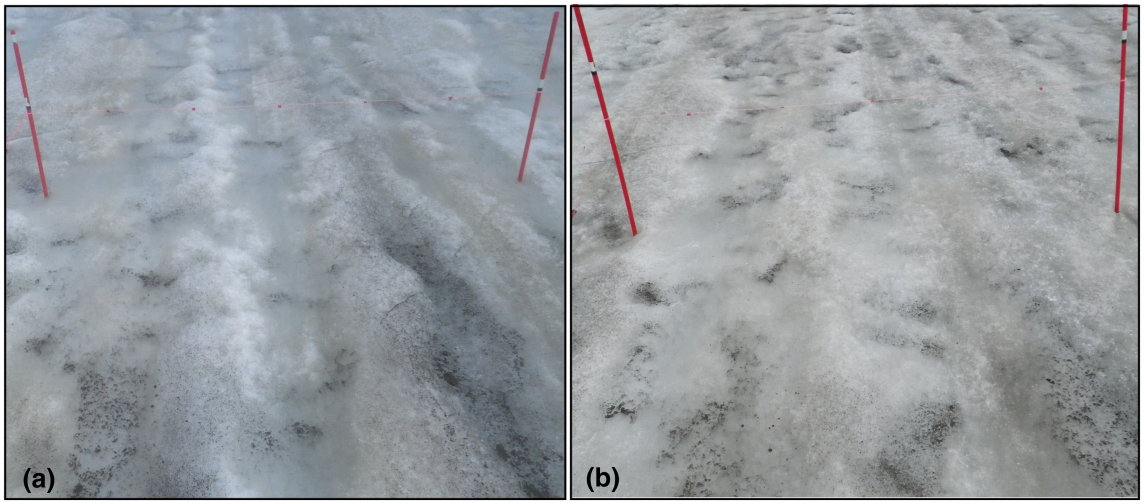

FIGURE 10 Images of the observation plot on (a) 31 July 31, DOY 212, and (b) 21 August, DOY 233 that reveal the down-glacier oriented foliation and brighter ice dominates surface morphology during OSP1 while during OSP2, a more complex 'island' topography develops, reducing the dominance of the down-glacier orientation of relative relief [Color figure can be viewed at wileyonlinelibrary.com]

The evolutionary sequence we illustrate above (Figure 3b–d) accords with the typical hydrological activation of an ablating glacier surface (Hambrey, 1977): sheetwash occurs on newly exposed ice with a proportion refreezing, and as melting proceeds, the meltwater flow initiates rills. As meltwater fluxes rise, this incipient drainage network then incises and develops. The maturing network is commonly influenced by surface slope and/or ice structure and becomes the antecedent topography for the following summer season. At Lower Foxfonna, during OSP2, the relatively low rate of ablation reduces the hydrologically-driven amplification of roughness generated through the establishment of a drainage network. This diminished development of surface topography is exacerbated by several intertwined factors: Foxfonna's dominantly cold thermal regime, which reduces the energy available for melt and to change topography through ablation; the relative balance between radiative fluxes that promote the formation of roughness elements; and the turbulent fluxes that, by acting on the topographic highs, can reduce roughness. Consequently, the ice surface remains defined by small scale rills, and a general decrease in anisotropy towards zero, despite an increase in both the directional z_0 metrics.

On the basis of our findings, we argue that the hydrology-roughness correlation, identified at a coarse scale by Rippin et al. (2015), may take two forms: firstly, down-glacier oriented topography aligned with structure and/or peak melt season hydrology; and secondly, topography generated by supraglacial rills that braid or anastomose. We hypothesize that the latter may be more common during cloudy periods with elevated turbulent energy fluxes, at least in cool Arctic summer conditions. Our dataset, owing to its brief duration and short singular synoptic time periods, did not allow us to robustly examine the role of turbulent energy fluxes in smoothing the glacier surface, as hypothesized by Müller and Keeler (1969). It remains unclear, therefore, whether during periods dominated by turbulent energy flux, a feedback exists wherein continued braiding of rills an associate ice ablation suppress the evolution of roughness, or whether the meltwater volumes produced enable rill coalescence, incision and the evolution of a rougher surface.

4.4 | Summary and wider relevance

We highlight that traditional morphometric measures (e.g., Wilson & Gallant, 2000) at fine-resolution are ineffective in providing insight into bare-ice topographic variability, in part owing to the comparatively smooth nature of ablating glacier ice in the absence of lager scale roughness features (e.g., Cathles et al., 2011; Dachauer et al., 2021). However, at the 25 mm kernel-scale our data revealed an inverse association between blue-band surface brightness and Riley's roughness index. With knowledge that the bearing area curves and *z*-score histograms revealed a near-surface variability and the blue-band albedo proxy offers a first-order discrimination between ice and impurities (Irvine-Fynn et al., 2010), the relationship invoked the melting in and emergence of impurities, respectively, increasing and decreasing albedo (e.g., Bøggild et al., 2010). Lower albedo impurities may also include meltwater, or the water column that exists within features such as cryoconite holes (e.g., Cook et al., 2016; Gribbon, 1979; Takeuchi et al., 2018). Consequently, it is important to note that the retrieval of ice surface topographic roughness metrics using photogrammetric techniques, including derivation of z_0 estimates, may require consideration of refraction through-water. Given the scale of features such as cryoconite holes and rills, such adjustments are most likely to have a small effect (Woodget et al., 2015). However, in energy transfer terms, the aerodynamic roughness length may, locally, be defined by the water surface, not the ice surface; therefore, in areas exhibiting a high frequency of rills or water-filled topographic lows including cryoconite holes, spatial or temporal variations in the near-surface or surface water table (Cook et al., 2016) may be an important consideration for defining seasonal and sub-seasonal patterns in z_0.

Further evidence of hydrological controls on bare-ice roughness was found in the temporal evolution of the plot's profile-based and two-dimensional roughness metrics. This evolution followed Smith et al.'s (2020) conceptual model, and highlighted that the degradation of superimposed ice results in the rapid decline in z_0 following the elimination of seasonal snow, while subsequent melt promotes a

subtle increase in roughness. The analysis of semivariograms revealed the superimposed ice phase exhibits topography defined by antecedent, slope- and/or structure-oriented features likely exploited by the hydrological activation of the surface. The presence or absence of superimposed ice may condition the magnitude, rate and duration of this initial bare-ice roughness decline. Then, as melt continues, and particularly under conditions of elevated turbulent energy fluxes, the bare-ice surface topography becomes characterized by the formation of braided rills and their development towards a parallel drainage network. It is unclear whether roughness stimulates rill geometry (e.g., Mantelli et al., 2015) or ice structure and hydrology define the spatial arrangement of roughness. With the specific form of topography critical to the frontal area exposed to the prevailing wind, transitions between aligned and braided forms influence the true aerodynamic roughness lengths, z_0, and emphasize the need to employ z_{0S} (Smith et al., 2016) to describe the surface characteristic. However, because this study reports a single site over a single melt season, separation of the coupled meteorological, ice structural and hydrological drivers remains equivocal and invites further study.

With evidence of hydrological controls underlying surface roughness, themselves associated with relative balances between radiative and turbulent energy drive ablation, we suggest the activation and evolution of supraglacial hydrology represents a primary control on bare-ice z_0. Variation in ablation regime and meltwater fluxes impacting on z_0 can explain the contrasting, unsystematic or indiscriminate trajectories of roughness either over time particularly at the plot-scale (e.g., Brock et al., 2006; Guo et al., 2018; Liu et al., 2020; Smith et al., 2020). Under melt regimes with relatively heightened turbulent energy fluxes, the maintenance of braided rills and micro-channels may supress z_0. Consequently, we suggest that in a warming climate, in both Arctic and Alpine settings, owing to potential changes in the ratios between turbulent and radiative energy fluxes: (i) the ablation-to-accumulation season transition may experience reductions in z_0, and (ii) the hydrological response of glacier surfaces will define their aerodynamic roughness trajectory, surface anisotropy, and the morphology inherited from one year to the next.

The advent of consumer-grade high-resolution imaging platforms, including uncrewed aerial vehicles, and photogrammetric software packages (e.g., Bash et al., 2018; Bash & Moorman, 2020; Rippin et al., 2015; Ryan et al., 2015, Ryan et al., 2017a) offers considerable opportunity to develop fine-scale bare-ice topographic time-series across multiple sites and years. Such data sets, and the analytical framework presented here, would facilitate (i) a refinement of the model of seasonal progression of surface roughness (Smith et al., 2020), including end-of-melt-season trajectories; (ii) an improved understanding of the relative significance of the energy balance components, ice structure, and rills or micro-channels in defining surface topography; and, (iii) better constraints on the retrieval of coarser-resolution satellite-derived measures, their variability and physical meaning. These are critical questions for improving projections of future glacier mass balance and seasonal runoff patterns in the Arctic and elsewhere, where snowlines are forecast to rise (e.g., Huss & Hock, 2015; Noël et al., 2019, 2020; Ryan et al., 2019; Žebre et al., 2021) and bare-ice extents and turbulent energy exchanges to increase, transiently on receding valley glaciers or more progressively around the margins of Greenland and Antarctica over the coming decades.

5 | CONCLUSIONS

Modelling studies have forecast an increase in the extent of bare glacier ice during the summer melt season in the Arctic over the next few decades as air temperatures rise. The warmer air can contribute to raising ice ablation as turbulent energy fluxes increase, which themselves are modulated by the ice surface topography and its aerodynamic roughness. Employing a novel time-lapse digital imaging and photogrammetry methodology at a High-Arctic site, we demonstrate fine-scale temporal evolution of ice topography over two 9-day melt-season periods. Our data showed that traditional kernel-based geomorphological metrics commonly used to describe roughness were not effective in revealing the temporal dynamics in ice surface topography that were evident in profile-based and two-dimensional metrics. The anisotropic ice surface evidenced a progressive decline followed by an increase in aerodynamic roughness at the millimetre scale. Using a geostatistical and spectral analysis of the surface topography we demonstrate that roughness variations relate to the vertical movement of impurities and hydrological activation of the ice surface. Over time, down-glacier oriented, superimposed ice ridges transitioned to a bare-ice surface characterized by braiding rills, which highlights the importance of supraglacial hydrology in modulating surface roughness. With forecasts of rising air temperatures, cloudiness and rainfall in Arctic latitudes, augmented turbulent energy fluxes may result in the increased prevalence of rill-dominated hydrology. Consequently, to better constrain seasonal and sub-seasonal trajectories of glacier topography to employ within numerical mass balance models, we suggest our analytical approach provides a framework for future studies using fine-scale DSMs. Assessments should exploit not only topographic time-series, but also integrate geostatistical analyses coupled with meteorological data to identify both time-variable process and form.

ACKNOWLEDGEMENTS

TDLI-F acknowledges The Leverhulme Trust (Grant: RF-2018-584/4) and The Climate Change Consortium of Wales (C3W). The University Centre in Svalbard (UNIS) is thanked for the logistical support of fieldwork. AJH and TDLI-F acknowledge The Royal Geographical Society – Peter Fleming Award, a National Geographic Research and Exploration grant and Store Norske Spitsbergen Kulkompani AS for the help in establishing the monitoring at Foxfonna. Support from TerraDat with Topcon's Image Master Pro was gratefully received by TDJ. TDLI-F thanks Jim Chandler for a late-night conversation at an 'Arolla project reunion' well over a decade ago suggesting that 'if there was enough texture maybe one commercial grade camera and some photogrammetry might reveal the topographic dynamics of an ice surface'. How the field developed! Pete Bunting is thanked for help adapting the energy balance model code, and Morgan Jones and Hywel Griffiths commented on earlier versions of the manuscript. Two anonymous reviewers are thanked for constructive feedback that improved the clarity of the article.

CONFLICT OF INTEREST

None.

DATA AVAILABILITY STATEMENT

The datasets generated during and/or analysed in this study are available in the Zenodo repository (https://doi.org/10.5281/zenodo.

5784564). The base energy balance model, in Python, is available at: https://github.com/atedstone/ebmodel.

ORCID

Tristram D. L. Irvine-Fynn https://orcid.org/0000-0003-3157-6646
Tom O. Holt https://orcid.org/0000-0001-8361-0688
Timothy D. James https://orcid.org/0000-0003-4082-7822
Mark W. Smith https://orcid.org/0000-0003-4361-9527
Nick Rutter https://orcid.org/0000-0002-5008-3575
Philip R. Porter https://orcid.org/0000-0001-5618-9189
Andrew J. Hodson https://orcid.org/0000-0002-1255-7987

REFERENCES

Allmaras, R.R., Burwell, R.E., Larson, W.E. & Holt, R.F. (1966) Total porosity and random roughness of the interrow zone as influenced by tillage. USDA Conservation Research Report, 7, 22 pp.

Arnold, N.S., Rees, W.G., Hodson, A.J. & Kohler, J. (2006) Topographic controls on the surface energy balance of a high Arctic valley glacier. *Journal of Geophysical Research - Earth Surface*, 111(F2), F02011. https://doi.org/10.1029/2005JF000426

Ascione, A., Cinque, A., Miccadei, E., Villani, F. & Berti, C. (2008) The Plio-Quaternary uplift of the Apennine chain: new data from the analysis of topography and river valleys in Central Italy. *Geomorphology*, 102(1), 105–118. https://doi.org/10.1016/j.geomorph.2007.07.022

Bash, E., Moorman, B. & Gunther, A. (2018) Detecting short-term surface melt on an Arctic glacier using UAV surveys. *Remote Sensing*, 10(10), 1547. https://doi.org/10.13390/rs10101547

Bash, E.A. & Moorman, B.J. (2020) Surface melt and the importance of water flow – an analysis based on high-resolution unmanned aerial vehicle (UAV) data for an Arctic glacier. *The Cryosphere*, 14(2), 549–563. https://doi.org/10.5194/tc-14-549-2020

Bintanja, R. (2018) The impact of Arctic warming on increased rainfall. *Scientific Reports*, 8(1), 1–6. https://doi.org/10.1038/s41598-018-34450-3

Bintanja, R., van der Wiel, K., Van der Linden, E.C., Reusen, J., Bogerd, L., Krikken, F. & Selten, F.M. (2020) Strong future increases in Arctic precipitation variability linked to poleward moisture transport. *Science Advances*, 6(7), eaax6869. https://doi.org/10.1126/sciadv.aax6869

Bøggild, C.E., Brandt, R.E., Brown, K.J. & Warren, S.G. (2010) The ablation zone in northeast Greenland: ice types, albedos and impurities. *Journal of Glaciology*, 56(195), 101–113. https://doi.org/10.3189/002214310791190776

Brasington, J., Vericat, D. & Rychkov, I. (2012) Modeling river bed morphology, roughness, and surface sedimentology using high resolution terrestrial laser scanning. *Water Resources Research*, 48(11), W11519. https://doi.org/10.1029/2012WR012223

Brock, B.W. & Arnold, N.S. (2000) A spreadsheet-based (Microsoft Excel) point surface energy balance model for glacier and snow melt studies. *Earth Surface Processes and Landforms*, 25(6), 649–658. https://doi.org/10.1002/1096-9837(200006)25:6<649::AID-ESP97>3.0.CO;2-U

Brock, B.W., Willis, I.C. & Sharp, M.J. (2006) Measurement and parameterization of aerodynamic roughness length variations at Haut Glacier d'Arolla, Switzerland. *Journal of Glaciology*, 52(177), 281–297. https://doi.org/10.3189/172756506781828746

van den Broeke, M., Box, J., Fettweis, X., Hanna, E., Noël, B., Tedesco, M., van As, D., van de Berg, W.J. & van Kampenhout, L. (2017) Greenland ice sheet surface mass loss: recent developments in observation and modeling. *Current Climate Change Reports*, 3(4), 345–356. https://doi.org/10.1007/s40641-017-0084-8

Cathles, L.M., Abbot, D.S., Bassis, J.N. & MacAyeal, D.R. (2011) Modeling surface-roughness/solar-ablation feedback: application to small-scale surface channels and crevasses of the Greenland ice sheet. *Annals of Glaciology*, 52(59), 99–108. https://doi.org/10.3189/172756411799096268

Chambers, J.R., Smith, M.W., Quincey, D.J., Carrivick, J.L., Ross, A.N. & James, M.R. (2020) Glacial Aerodynamic roughness estimates: uncertainty, sensitivity, and precision in field measurements. *Journal of Geophysical Research - Earth Surface*, 125(2), e2019JF005167.

Chambers, J.R., Smith, M.W., Smith, T., Sailer, R., Quincey, D.J., Carrivick, J.L., Nicholson, L., Mertes, J., Stiperski, I. & James, M.R. (2021) Correcting for systematic underestimation of topographic glacier aerodynamic roughness values from Hintereisferner, Austria. *Frontiers in Earth Science*, 9, 691195. https://doi.org/10.3389/feart.2021.691195

Chandler, D.M., Alcock, J.D., Wadham, J.L., Mackie, S.L. & Telling, J. (2015) Seasonal changes of ice surface characteristics and productivity in the ablation zone of the Greenland Ice Sheet. *The Cryosphere*, 9(2), 487–504. https://doi.org/10.5194/tc-9-487-2015

Christiansen, H.H., French, H.M. & Humlum, O. (2005) Permafrost in the Gruve-7 mine, Adventdalen, Svalbard. *Norsk Geografisk Tidsskrift*, 59(2), 109–115. https://doi.org/10.1080/00291950510020592

Cook, J.M., Hodson, A.J. & Irvine-Fynn, T.D. (2016) Supraglacial weathering crust dynamics inferred from cryoconite hole hydrology. *Hydrological Processes*, 30(3), 433–446. https://doi.org/10.1002/hyp.10602

Cuffey, K.M. & Paterson, W.S.B. (2010) *The physics of glaciers*, 4th edition, Oxford: Butterworth-Heinemann.

Curley, A.N., Kochtitzky, W.H., Edwards, B.R. & Copland, L. (2021) Glacier changes over the past 144 years at Alexandra Fiord, Ellesmere Island, Canada. *Journal of Glaciology*, 67(263), 511–522. https://doi.org/10.1017/jog.2021.4

Currence, H.D. & Lovely, W.G. (1970) The analysis of soil surface roughness. *Transactions of ASAE*, 13(6), 710–714. https://doi.org/10.13031/2013.38702

Dachauer, A., Hann, R. & Hodson, A.J. (2021) Aerodynamic roughness length of crevassed tidewater glaciers from UAV mapping. *The Cryosphere*, 15(12), 5513–5528. https://doi.org/10.5194/tc-15-5513-2021

Doyle, S.H., Hubbard, A., van De Wal, R.S., Box, J.E., van As, D., Scharrer, K., Meierbachtol, T.W., Smeets, P.C., Harper, J.T., Johansson, E. & Mottram, R.H. (2015) Amplified melt and flow of the Greenland ice sheet driven by late-summer cyclonic rainfall. *Nature Geoscience*, 8(8), 647–653. https://doi.org/10.1038/ngeo2482

Fausto, R.S., van As, D., Box, J.E., Colgan, W., Langen, P.L. & Mottram, R.H. (2016) The implication of nonradiative energy fluxes dominating Greenland ice sheet exceptional ablation area surface melt in 2012. *Geophysical Research Letters*, 43(6), 2649–2658. https://doi.org/10.1002/2016GL067720

Fitzpatrick, N., Radić, V. & Menounos, B. (2019) A multi-season investigation of glacier surface roughness lengths through in situ and remote observation. *The Cryosphere*, 13(3), 1051–1071. https://doi.org/10.5194/tc-13-1051-2019

Giesen, R.H., Andreassen, L.M., Oerlemans, J. & Van Den Broeke, M.R. (2014) Surface energy balance in the ablation zone of Langfjordjøkelen, an Arctic, maritime glacier in northern Norway. *Journal of Glaciology*, 60(219), 57–70. https://doi.org/10.3189/2014JoG13J063

Gillett, S. & Cullen, N.J. (2011) Atmospheric controls on summer ablation over Brewster Glacier, New Zealand. *International Journal of Climatology*, 31(13), 2033–2048. https://doi.org/10.1002/joc.2216

Greuell, W. & de Wildt, M.D.R. (1999) Anisotropic reflection by melting glacier ice: measurements and parametrizations in Landsat TM bands 2 and 4. *Remote Sensing of Environment*, 70(3), 265–277. https://doi.org/10.1016/S0034-4257(99)00043-7

Gribbon, P.W.F. (1979) Cryoconite holes on Sermikavsak, west Greenland. *Journal of Glaciology*, 22(86), 177–181. https://doi.org/10.1017/S0022143000014167

Guo, S., Chen, R., Liu, G., Han, C., Song, Y., Liu, J., Yang, Y., Liu, Z., Wang, X., Liu, X. & Wang, L. (2018) Simple parameterization of aerodynamic roughness lengths and the turbulent heat fluxes at the top

of midlatitude August-One Glacier, Qilian Mountains, China. *Journal of Geophysical Research-Atmospheres*, 123(21), 12–066. https://doi.org/10.1029/2018JD028875

Guo, X., Yang, K., Zhao, L., Yang, W., Li, S., Zhu, M., Yao, T. & Chen, Y. (2011) Critical evaluation of scalar roughness length parametrizations over a melting valley glacier. *Boundary-Layer Meteorology*, 139(2), 307–332. https://doi.org/10.1007/s10546-010-9586-9

Hambrey, M.J. (1977) Supraglacial drainage and its relationship to structure, with particular reference to Charles Rabots Bre, Okstindan, Norway. *Norsk Geografisk Tidsskrift*, 31(2), 69–77. https://doi.org/10.1080/00291957708545319

Hambrey, M.J. & Lawson, W. (2000) Structural styles and deformation fields in glaciers: a review. *Geological Society Special Publication*, 176(1), 59–83. https://doi.org/10.1144/GSL.SP.2000.176.01.06

Hanssen-Bauer, I., Førland, E.J., Hisdal, H., Mayer, S., Sandø, A.B. & Sorteberg, A. (2019) Climate in Svalbard 2100. A knowledge base for climate. Norwegian Centre for Climate Services (NCCS) Report no. 1/2019. pp. 208.

Hanssen-Bauer, I., Kristensen Solås, M. & Steffensen, E.L. The climate of Spitsbergen. Klima, Norwegian Meteorological Institute Report 39/90, pp. 1–40.

Hay, J.E. & Fitzharris, B.B. (1988) A comparison of the energy-balance and bulk-aerodynamic approaches for estimating glacier melt. *Journal of Glaciology*, 34(117), 145–153. https://doi.org/10.1017/S0022143000032172

Herzfeld, U.C., Box, J.E., Steffen, K., Mayer, H., Caine, N. & Losleben, M.V. (2003) A case study on the influence of snow and ice surface roughness on melt energy. *Zeitschrift Fur Gletscherkunde Und Glazialgeologie*, 39, 1–42.

Herzfeld, U.C., Mayer, H., Feller, W. & Mimler, M. (2000) Geostatistical analysis of glacier-roughness data. *Annals of Glaciology*, 30, 235–242. https://doi.org/10.3189/172756400781820769.

Hock, R. (2005) Glacier melt: a review of processes and their modelling. *Progress in Physical Geography*, 29(3), 362–391. https://doi.org/10.1191/0309133305pp453ra

Hudleston, P.J. (2015) Structures and fabrics in glacial ice: A review. *Journal of Structural Geology*, 81, 1–27. https://doi.org/10.1016/j.jsg.2015.09.003

Huss, M. & Hock, R. (2015) A new model for global glacier change and sea-level rise. *Frontiers in Earth Science*, 3, 54. https://doi.org/10.3389/feart.2015.00054

Irvine-Fynn, T.D., Bridge, J.W. & Hodson, A.J. (2010) Rapid quantification of cryoconite: granule geometry and in situ supraglacial extents, using examples from Svalbard and Greenland. *Journal of Glaciology*, 56(196), 297–308. https://doi.org/10.3189/002214310791968421

Irvine-Fynn, T.D., Bridge, J.W. & Hodson, A.J. (2011) In situ quantification of supraglacial cryoconite morphodynamics using time-lapse imaging: an example from Svalbard. *Journal of Glaciology*, 57(204), 651–657. https://doi.org/10.3189/002214311797409695

Irvine-Fynn, T.D., Hanna, E., Barrand, N.E., Porter, P.R., Kohler, J. & Hodson, A.J. (2014a) Examination of a physically based, high-resolution, distributed Arctic temperature-index melt model, on Midtre Lovénbreen, Svalbard. *Hydrological Processes*, 28(1), 134–149. https://doi.org/10.1002/hyp.9526

Irvine-Fynn, T.D., Sanz-Ablanedo, E., Rutter, N., Smith, M.W. & Chandler, J.H. (2014b) Measuring glacier surface roughness using plot-scale, close-range digital photogrammetry. *Journal of Glaciology*, 60(223), 957–969. https://doi.org/10.3189/2014JoG14J032

James, T.D., Carbonneau, P.E. & Lane, S.N. (2007) Investigating the effects of DEM error in scaling analysis. *Photogrammetric Engineering & Remote Sensing*, 73(1), 67–78. https://doi.org/10.14358/PERS.73.1.67

Jenness, J. (2006) Topographic Position Index (tpi_jen.avx) extension for ArcView 3.x, v. 1.3a. Jenness Enterprises. Available at: http://www.jennessent.com/arcview/tpi.htm

Jennings, S.J.A. & Hambrey, M.J. (2021) Structures and deformation in glaciers and ice sheets. *Reviews of Geophysics*, 59(3), e2021RG000743. https://doi.org/10.1029/2021RG000743

Journel, A.G. & Huijbregts, C.J. (1978) *Mining Geostatistics*. New York: Academic Press.

Koziol, K.A., Moggridge, H.L., Cook, J.M. & Hodson, A.J. (2019) Organic carbon fluxes of a glacier surface: A case study of Foxfonna, a small Arctic glacier. *Earth Surface Processes and Landforms*, 44(2), 405–416. https://doi.org/10.1002/esp.4501

Leidman, S., Rennermalm, Å.K., Lathrop, R.G. & Cooper, M. (2021) Terrain-based shadow correction method for assessing supraglacial features on the Greenland Ice Sheet. *Frontiers in Remote Sensing*, 2, 690474. https://doi.org/10.3389/frsen.2021.690474

Liestøl, O. (1974) Glaciological work in 1972. In: *Norsk Polarinstitutt Årbok 1972*. Oslo: Norsk Polarinstitutt, pp. 125–135.

Lindsay, J.B., Cockburn, J.M.H. & Russell, H.A.J. (2015) An integral image approach to performing multi-scale topographic position analysis. *Geomorphology*, 245, 51–61. https://doi.org/10.1016/j.geomorph.2015.05.025

Lindsay, J.B., Newman, D.R. & Francioni, A. (2019) Scale-optimized surface roughness for topographic analysis. *Geosciences*, 9(7), 322. https://doi.org/10.3390/geosciences9070322

Liu, J., Chen, R. & Han, C. (2020) Spatial and temporal variations in glacier aerodynamic surface roughness during the melting season, as estimated at the August-One ice cap, Qilian mountains, China. *The Cryosphere*, 14(3), 967–984. https://doi.org/10.5194/tc-14-967-2020

Mantelli, E., Camporeale, C. & Ridolfi, L. (2015) Supraglacial channel inception: Modeling and processes. *Water Resources Research*, 51(9), 7044–7063. https://doi.org/10.1002/2015WR017075

Martín-Español, A., Navarro, F.J., Otero, J., Lapazaran, J.J. & Błaszczyk, M. (2015) Estimate of the total volume of Svalbard glaciers, and their potential contribution to sea-level rise, using new regionally based scaling relationships. *Journal of Glaciology*, 61(225), 29–41. https://doi.org/10.3189/2015JoG14J159

Middlemas, E.A., Kay, J.E., Medeiros, B.M. & Maroon, E.A. (2020) Quantifying the influence of cloud radiative feedbacks on Arctic surface warming using cloud locking in an Earth system model. *Geophysical Research Letters*, 47(15), e2020GL089207. https://doi.org/10.1029/2020GL089207

Mulla, D.J. (1988) Using geostatistics and spectral analysis to study spatial patterns in the topography of southeastern Washington State, USA. *Earth Surface Processes and Landforms*, 13(5), 389–405. https://doi.org/10.1002/esp.3290130505

Müller, F. & Keeler, C.M. (1969) Errors in short-term ablation measurements on melting ice surfaces. *Journal of Glaciology*, 8(52), 91–105. https://doi.org/10.1017/S0022143000020785

Munro, D.S. (1989) Surface roughness and bulk heat transfer on a glacier: comparison with eddy correlation. *Journal of Glaciology*, 35(121), 343–348. https://doi.org/10.1017/S0022143000009266

Nield, J.M., Chiverrell, R.C., Darby, S.E., Leyland, J., Vircavs, L.H. & Jacobs, B. (2013) Complex spatial feedbacks of tephra redistribution, ice melt and surface roughness modulate ablation on tephra covered glaciers. *Earth Surface Processes and Landforms*, 38(1), 95–102. https://doi.org/10.1002/esp.3352

Noël, B., Jakobs, C.L., van Pelt, W.J.J., Lhermitte, S., Wouters, B., Kohler, J., Hagen, J.O., Luks, B., Reijmer, C.H., van de Berg, W.J. & van den Broeke, M.R. (2020) Low elevation of Svalbard glaciers drives high mass loss variability. *Nature Communications*, 11(1), 1–8. https://doi.org/10.1038/s41467-020-18356-1

Noël, B., van de Berg, W.J., Lhermitte, S. & van den Broeke, M.R. (2019) Rapid ablation zone expansion amplifies north Greenland mass loss. *Science Advances*, 5(9), eaaw0123. https://doi.org/10.1126/sciadv.aaw0123

Østby, T.I., Schuler, T.V., Hagen, J.O., Hock, R., Kohler, J. & Reijmer, C.H. (2017) Diagnosing the decline in climatic mass balance of glaciers in Svalbard over 1957–2014. *The Cryosphere*, 11(1), 191–215. https://doi.org/10.5194/tc-11-191-2017

Overland, J., Dunlea, E., Box, J.E., Corell, R., Forsius, M., Kattsov, V., Olsen, M.S., Pawlak, J., Reiersen, L.O. & Wang, M. (2019) The urgency of Arctic change. *Polar Science*, 21, 6–13. https://doi.org/10.1016/j.polar.2018.11.008

Perron, J.T., Kirchner, J.W. & Dietrich, W.E. (2008) Spectral signatures of characteristic spatial scales and nonfractal structure in landscapes. *Journal of Geophysical Research - Earth Surface*, 113(F4), F04003.

Pyrcz, M.J. & Deutsch, C.V. (2003) The whole story on the hole effect. *Geostatistical Association of Australasia Newsletter*, 18, 3–5.

Rees, W.G. & Arnold, N.S. (2006) Scale-dependent roughness of a glacier surface: implications for radar backscatter and aerodynamic roughness modelling. *Journal of Glaciology*, 52(177), 214–222. https://doi.org/10.3189/172756506781828665

Riley, S.J., DeGloria, S.D. & Elliot, R. (1999) Index that quantifies topographic heterogeneity. *Intermountain Journal of Sciences*, 5(1–4), 23–27.

Rippin, D.M., Pomfret, A. & King, N. (2015) High resolution mapping of supra-glacial drainage pathways reveals link between micro-channel drainage density, surface roughness and surface reflectance. *Earth Surface Processes and Landforms*, 40(10), 1279–1290. https://doi.org/10.1002/esp.3719

Romkens, M.J. & Wang, J.Y. (1986) Effect of tillage on surface roughness. *Transactions of ASAE*, 29(2), 429–0433. https://doi.org/10.13031/2013.30167

Rossini, M., Di Mauro, B., Garzonio, R., Baccolo, G., Cavallini, G., Mattavelli, M., De Amicis, M. & Colombo, R. (2018) Rapid melting dynamics of an alpine glacier with repeated UAV photogrammetry. *Geomorphology*, 304, 159–172. https://doi.org/10.1016/j.geomorph.2017.12.039

Rutter, N., Hodson, A., Irvine-Fynn, T. & Solås, M.K. (2011) Hydrology and hydrochemistry of a deglaciating high-Arctic catchment, Svalbard. *Journal of Hydrology*, 410(1–2), 39–50. https://doi.org/10.1016/j.jhydrol.2011.09.001

Ryan, J.C., Hubbard, A., Box, J.E., Brough, S., Cameron, K., Cook, J.M., Cooper, M., Doyle, S.H., Edwards, A., Holt, T. & Irvine-Fynn, T. (2017a) Derivation of high spatial resolution albedo from UAV digital imagery: application over the Greenland Ice Sheet. *Frontiers in Earth Science*, 5, 40. https://doi.org/10.3389/feart.2017.00040

Ryan, J.C., Hubbard, A.L., Box, J.E., Todd, J., Christoffersen, P., Carr, J.R., Holt, T.O. & Snooke, N. (2015) UAV photogrammetry and structure from motion to assess calving dynamics at Store Glacier, a large outlet draining the Greenland ice sheet. *The Cryosphere*, 9(1), 1–11. https://doi.org/10.15194/tc-9-1-2015

Ryan, J.C., Hubbard, A., Irvine-Fynn, T.D., Doyle, S.H., Cook, J.M., Stibal, M. & Box, J.E. (2017b) How robust are in situ observations for validating satellite-derived albedo over the dark zone of the Greenland Ice Sheet? *Geophysical Research Letters*, 44(12), 6218–6225. https://doi.org/10.1002/2017GL073661

Ryan, J.C., Smith, L.C., Van As, D., Cooley, S.W., Cooper, M.G., Pitcher, L.H. & Hubbard, A. (2019) Greenland Ice Sheet surface melt amplified by snowline migration and bare ice exposure. *Science Advances*, 5(3), eaav3738. https://doi.org/10.1126/sciadv.aav3738

Schneider, C.A., Rasband, W.S. & Eliceiri, K.W. (2012) NIH Image to ImageJ: 25 years of image analysis. *Nature Methods*, 9(7), 671–675. https://doi.org/10.1038/nmeth.2089

Smeets, C.J.P.P., Duynkerke, P.G. & Vugts, H.F. (1999) Observed wind profiles and turbulence fluxes over an ice surface with changing surface roughness. *Boundary-Layer Meteorology*, 92(1), 99–121. https://doi.org/10.1023/A:1001899015849

Smeets, C.J.P.P. & van den Broeke, M.R. (2008) Temporal and spatial variations of the aerodynamic roughness length in the ablation zone of the Greenland ice sheet. *Boundary-Layer Meteorology*, 128(3), 315–338. https://doi.org/10.1007/s10546-008-9291-0

Smith, M.W. (2014) Roughness in the earth sciences. *Earth-Science Reviews*, 136, 202–225. https://doi.org/10.1016/j.earscirev.2014.05.016

Smith, M.W., Quincey, D.J., Dixon, T., Bingham, R.G., Carrivick, J.L., Irvine-Fynn, T.D. & Rippin, D.M. (2016) Aerodynamic roughness of glacial ice surfaces derived from high-resolution topographic data. *Journal of Geophysical Research - Earth Surface*, 121(4), 748–766. https://doi.org/10.1002/2015JF003759

Smith, B.E., Raymond, C.F. & Scambos, T. (2006) Anisotropic texture of ice sheet surfaces. *Journal of Geophysical Research - Earth Surface*, 111(F1), F01019. https://doi.org/10.1029/2005JF000393

Smith, T., Smith, M.W., Chambers, J.R., Sailer, R., Nicholson, L., Mertes, J., Quincey, D.J., Carrivick, J.L. & Stiperski, I. (2020) A scale-dependent model to represent changing aerodynamic roughness of ablating glacier ice based on repeat topographic surveys. *Journal of Glaciology*, 66(260), 950–964. https://doi.org/10.1017/jog.2020.56

Smith, M.W. & Vericat, D. (2015) From experimental plots to experimental landscapes: topography, erosion and deposition in sub-humid badlands from structure-from-motion photogrammetry. *Earth Surface Processes and Landforms*, 40(12), 1656–1671. https://doi.org/10.1002/esp.3747

Spagnolo, M., Bartholomaus, T.C., Clark, C.D., Stokes, C.R., Atkinson, N., Dowdeswell, J.A., Ely, J.C., Graham, A.G., Hogan, K.A., King, E.C. & Larter, R.D. (2017) The periodic topography of ice stream beds: Insights from the Fourier spectra of mega-scale glacial lineations. *Journal of Geophysical Research - Earth Surface*, 122(7), 1355–1373. https://doi.org/10.1002/2016JF004154

Takeuchi, N., Sakaki, R., Uetake, J., Nagatsuka, N., Shimada, R., Niwano, M. & Aoki, T. (2018) Temporal variations of cryoconite holes and cryoconite coverage on the ablation ice surface of Qaanaaq Glacier in northwest Greenland. *Annals of Glaciology*, 59(77), 21–30. https://doi.org/10.1017/aog.2018.19

Tedstone, A.J., Cook, J.M., Williamson, C.J., Hofer, S., McCutcheon, J., Irvine-Fynn, T., Gribbin, T. & Tranter, M. (2020) Algal growth and weathering crust state drive variability in western Greenland Ice Sheet ice albedo. *The Cryosphere*, 14(2), 521–538. https://doi.org/10.5194/tc-14-521-2020

Telling, J., Anesio, A.M., Tranter, M., Stibal, M., Hawkings, J., Irvine-Fynn, T., Hodson, A., Butler, C., Yallop, M. & Wadham, J. (2012) Controls on the autochthonous production and respiration of organic matter in cryoconite holes on high Arctic glaciers. *Journal of Geophysical Research – Biogeosciences*, 117(G1), G01017.

van Pelt, W.J.J., Kohler, J., Liston, G.E., Hagen, J.O., Luks, B., Reijmer, C.H. & Pohjola, V.A. (2016) Multidecadal climate and seasonal snow conditions in Svalbard. *Journal of Geophysical Research: Earth Surface*, 121(11), 2100–2117. https://doi.org/10.1002/2016jf003999

van Tiggelen, M., Smeets, P.C., Reijmer, C.H., Wouters, B., Steiner, J.F., Nieuwstraten, E.J., Immerzeel, W.W. & van den Broeke, M.R. (2021) Mapping the aerodynamic roughness of the Greenland ice sheet surface using ICESat-2: Evaluation over the K-transect. *The Cryosphere*, 15(6), 2601–2621. https://doi.org/10.5194/tc-15-2601-2021

Wackrow, R. & Chandler, J.H. (2008) A convergent image configuration for DEM extraction that minimises the systematic effects caused by an inaccurate lens model. *The Photogrammetric Record*, 23(121), 6–18. https://doi.org/10.1111/j.1477-9730.2008.00467.x

Wadham, J.L. & Nuttall, A.M. (2002) Multiphase formation of superimposed ice during a mass-balance year at a maritime high-Arctic glacier. *Journal of Glaciology*, 48(163), 545–551. https://doi.org/10.3189/172756502781831025

Willis, I.C., Arnold, N.S. & Brock, B.W. (2002) Effect of snowpack removal on energy balance, melt and runoff in a small supraglacial catchment. *Hydrological Processes*, 16(14), 2721–2749. https://doi.org/10.1002/hyp.1067

Wilson, J.P. & Gallant, J.C. (Eds). (2000) *Digital terrain analysis. Terrain analysis: Principles and applications*. New York: John Wiley & Sons, p. 520.

Wolf, P.R. & Dewitt, B.A. (2000) *Elements of Photogrammetry, with Applications in GIS*. New York: McGraw-Hill, p. 608.

Woodget, A.S., Carbonneau, P.E., Visser, F. & Maddock, I.P. (2015) Quantifying submerged fluvial topography using hyperspatial resolution UAS imagery and structure from motion photogrammetry. *Earth Surface Processes and Landforms*, 40(1), 47–64. https://doi.org/10.1002/esp.3613

Žebre, M., Colucci, R.R., Giorgi, F., Glasser, N.F., Racoviteanu, A.E. & Del Gobbo, C. (2021) 200 years of equilibrium-line altitude variability across the European Alps (1901–2100). *Climate Dynamics*, 56(3), 1183–1201. https://doi.org/10.1007/s00382-020-05525-7

How to cite this article: Irvine-Fynn, T.D.L., Holt, T.O., James, T.D., Smith, M.W., Rutter, N., Porter, P.R. et al. (2022) Time-lapse photogrammetry reveals hydrological controls of fine-scale High-Arctic glacier surface roughness evolution. *Earth Surface Processes and Landforms*, 47(6), 1635–1652. Available from: https://doi.org/10.1002/esp.5339